8-2-2003

Estimation of Soil Moisture Using Active Microwave Remote Sensing

Vinod Ramnath

Recommended Citation

Ramnath, Vinod, "Estimation of Soil Moisture Using Active Microwave Remote Sensing" (2003). *Theses and Dissertations*. 1937.
https://scholarsjunction.msstate.edu/td/1937

ESTIMATION OF SOIL MOISTURE USING ACTIVE MICROWAVE REMOTE SENSING

By

Vinod K. Ramnath

A Thesis
Submitted to the Faculty of
Mississippi State University
In Partial Fulfillment of the Requirements
for the Degree of Master of Science
in Electrical Engineering
in the Department of Electrical & Computer Engineering

Mississippi State, Mississippi

August, 2003

ESTIMATION OF SOIL MOISTURE USING ACTIVE MICROWAVE REMOTE SENSING

By

Vinod K. Ramnath

Approved:

Roger L. King
Giles Distinguished Professor of
Electrical and Computer Engineering
(Director of Thesis)

Jiancheng Shi
Assistant Researcher,
ICESS, University of California, Santa
Barbara
(Committee Member)

Michael S. Cox
Associate Professor of Plant & Soil
Sciences
(Committee Member)

J. Patrick Donohoe
Professor of Electrical and Computer
Engineering
(Committee Member)

Nicholas H. Younan
Graduate Program Coordinator of the
Department of Electrical & Computer
Engineering

A. Wayne Bennett
Dean of the College of
Engineering

Name: Vinod K. Ramnath

Date of Degree: August 2, 2003

Institution: Mississippi State University

Major Field: Electrical Engineering

Major Professor: Dr. Roger L. King

Title of Study: ESTIMATION OF SOIL MOISTURE USING ACTIVE MICROWAVE REMOTE SENSING

Pages in Study: 81

Candidate for Degree of Master of Science

The method for developing a soil moisture inversion algorithm using Radar data can be approached in two ways: the multiple-incident angle approach and the change detection method. This thesis discusses how these two methods can be used to predict surface soil moisture. In the multiple incident angle approach, surface roughness can be mapped, if multiple incident angle viewing is possible and if the surface roughness is assumed constant during data acquisitions. A backpropagation neural network (NN) is trained with the data set generated by the Integral Equation Method (IEM) model. The training data set includes possible combinations of backscatter obtained as a result of variation in dielectric constant within the period of data acquisitions. The inputs to the network are backscatter acquired at different incident angles. The outputs are correlation length and root mean square height (*rms*). Once the roughness is mapped using these

outputs, dielectric constant can be determined. Three different data sets, (backscatter acquired from multiple-frequencies, multiple-polarizations, and multiple-incident angles) are used to train the NN. The performance of the NN trained by the different data sets is compared.

The next approach is the application of the change detection concept. In this approach, the relative change in dielectric constant over two different periods is determined from Radarsat data using a simplified algorithm. The vegetation backscatter contribution can be removed with the aid of multi-spectral data provided by Landsat. A method is proposed that minimizes the effect of incident angle on Radar backscatter by normalizing the acquired SAR images to a reference angle. A quantitative comparison of some of the existing soil moisture estimation algorithms is also made

DEDICATION

I would like to dedicate this research to my parents and my brother whose constant support and encouragement made this work possible.

ACKNOWLEDGMENTS

I sincerely express my gratitude to my advisor Dr. Roger. L. King for his guidance and unrelenting support throughout my research work. His motivation and energy has always been a driving force for successful completion of this thesis work. I am indebted to Dr. Jiancheng Shi, (University of California, Santa Barbara) for supporting my thesis work with his suggestions and advices, and for providing me the RADARSAT data.

I would like to thank Dr. Michael Cox, and Dr. J. Patrick Donohoe for serving in my thesis committee. I would like to thank Dr. Michael Cosh (USDA) & Dr. T. J. Jackson (USDA) for providing me the required LANDSAT image. I would like to acknowledge NASA for funding my research.

TABLE OF CONTENTS

LIST OF TABLES

LIST OF FIGURES

FIGURE Page

FIGURE Page

CHAPTER I

INTRODUCTION

1.1 OVERVIEW

The need for estimation of soil moisture may differ from an agriculturist's, meteorologist's, or a water reservoir manager's standpoint of view. This thesis is limited to the estimation of soil moisture contained in the range (1 cm –5 cm) because of the penetration limits of radar. The moisture in these depths is generally referred to as surface soil moisture. Soil moisture is a constituent in the interface between atmosphere and land surface, or rather in the conversion of the radiant energy from the atmosphere into latent heat. Understanding these conversions and interpreting them meaningfully are the greatest challenges in hydrological sciences. Soil moisture plays an important role in the prediction of weather patterns, management of water reservoirs, providing early warning of droughts and floods, providing irrigation schedules and crop yields. Reference [1], defines soil moisture as the key boundary that influences the precipitation pattern in the southern great plains and the second most significant function in the mid-latitude continental regions. Hence, the role of soil moisture is important at both global and local scales, even though its volume is small compared to other components in the hydrological cycle [1], [2].

Soil moisture is a difficult parameter to measure because of its temporal variation. Soil moisture estimation using ground-based instruments are point measurements and thus, cannot be used in the above mentioned global or regional applications because of the varying nature of soil moisture on a large scale. Space based remote sensing is projected to be the solution to overcome the problems of ground based estimation of soil moisture. An effort of more than two decades has been invested in the development of efficient algorithms for soil moisture estimation using remote sensing. Sensors operating in the visible region can provide us with some information regarding soil moisture since the color and the texture of soil are dependent on the levels of soil moisture. Microwave region offers the best potential to derive soil moisture maps and was found as early as 1974 [3]. The most popular frequency bands in the microwave region are P, L, C and X bands for this application.

Remote sensing in the microwave band can be classified into active and passive remote sensing. Passive systems use the Sun as their source of microwave energy and are known as radiometers, whereas active systems have their own source and are known as radar. The detection of soil moisture for passive systems is based on the fact that emission of microwave energy is proportional to the product of surface temperature and surface emissivity, which in turn are dependent on the moisture content. This microwave energy is termed as brightness temperature. Active microwave remote sensing offers several advantages over passive sensing such as its ability to penetrate cloud cover (making it an all weather sensor), moderate penetration of vegetation cover, independent source of energy, and strong function of dielectric constant.

A series of soil moisture experiments were conducted during the past decade. The first major soil moisture campaign is what is known as the *Washita'94* experiment. The experiment acquired SIR-C (Shuttle Imaging Radar) measurements over Little

Watershed, Oklahoma during April 94. This experiment realized soil moisture validation with ground truth realizable from the Synthetic Aperture Radar (SAR) perspective. The Southern Great Plains Experiment in 1999 (*SPG99*) was aimed at providing aircraft data sets for algorithm development. Soil Moisture Experiment 2002 (*Smex02*), was designed for development of soil moisture products from several satellite sensors like the Aqua Advanced Scanning Microwave Radiometer (ASMR), Radarsat, and aircraft remote sensing instruments. Ground based observations were also set up for validation of the soil moisture products developed. The study region was Walnut Creek, a watershed located southwest of Ames, Iowa.

Radar data can be further classified as image and non-imaging radars. SARs, like the Canadian Radarsat belong to high resolution imaging radars and scatterometers, like the European ERS-1, belong to the non-imaging radars. Radar detects the microwave energy or the Radar backscatter (σ), as a result of scattering from the surface. The amount of the backscatter depends mainly on the dielectric constant (ε) of the soil medium and the surface parameters such as the *rms* height (h), correlation length (l), vegetation cover and the incident angle (θ). The ε is related to soil moisture through an empirical relation which is a function of soil texture. Soil texture is defined in terms of volume fractions of clay, sand and silt present in soil. Due to the dependency of σ on so many parameters, formulation of an inverse algorithm for soil moisture estimation is often referred to as an *ill posed problem*. The limitations posed by SAR imagery are its inability to simultaneously view the region of interest with different combinations of polarization, frequency and incident angle.

Most of the researches undertaken in the past have considered only bare pixels and sparsely covered vegetation pixels for generating soil moisture maps. All other pixels are usually masked using vegetation indices such as NDVI (Normalized Difference Vegetation Index). Since the presently available SARs (Radarsat, ERS-1) are capable of acquiring only single polarized data, there is a need to develop an inversion algorithm based on single polarized data. HH polarized waves have more interactions with the surface and are less attenuated by vegetation compared to VV polarization. Radarsat, because of its frequency of revisits and its ability to acquire HH polarized data, is a more effective tool. The objective of the thesis is to develop an inverse algorithm for soil moisture estimation from Radarsat SAR data. Radarsat operates at C band (5.3 GHz) with a resolution of 25m for the standard beam mode and a resolution of 8 m for the fine mode.

1.2 THESIS STRUCTURE

This thesis is structured as follows: Definitions of different parameters along with the relationship between dielectric constant, volumetric soil moisture and radar backscatter are presented in Chapter 2. Chapter 3 discusses the site characteristics, procedure for retrieving ground parameters from the site and processing of the SAR data. The chapter is an introduction to two soil moisture campaigns: *Washita'94 & Smex02,* and no attempt is taken to discuss these campaigns in detail. Chapter 4 is a review and comparison of the existing theoretical and empirical models.

The main challenges in the inversion algorithm have been incident angle correction and removal of backscatter effects due to vegetation. The SAR images acquired at different incident angles can be normalized to a reference angle, at least from the Integral Equation Method (IEM) model standpoint and is discussed in chapter 5. It is impossible to eliminate the contributions due to vegetation from the total backscatter using Radarsat alone. With the aid of visual imagery provided by Landsat, this unwanted term could be minimized to some extent. It is impractical to apply the IEM model to SAR acquired images due to the large volume of data and the algorithm's complexity. Chapter 5 deals with how the IEM model can be simplified using regression. The behavior of the coefficients with surface parameters as a result of regression is discussed. Neural networks (NN) trained by backpropagation algorithm have proved to be an effective tool for non-linear inversion problems. Radarsat has a revisit frequency over the same ROI (Region of Interest) that is a function of the beam mode. Therefore, this variable revisit frequency of visit of Radarsat can be exploited in the development of the algorithm and training data set for the NN. Finally, Chapter 6 is a summary and suggestions for future soil moisture field campaigns.

CHAPTER II

DEFINITIONS & RELATIONSHIPS OF DIFFERENT PARAMETERS

2.1 DIELECTRIC PROPERTY OF SOIL MEDIUM

Water is a permanent dipole because of its triangular molecular structure. Any molecule that has separation between positive and negative charges has a dipole moment. When an electric field is applied water molecules tend to align with the field. This phenomenon is known as polarization. The hydrogen-bonded network of the water molecule tends to oppose this alignment. This degree of opposition is known as dielectric constant [4]. From an electromagnetic wave perspective, the soil medium can be divided into free water, bound water, air, and bulk soil based on their distinctive dielectric properties [5]. For instance, bound water interacts with an electromagnetic wave differently than free water because of the amount of water held by the soil particles. So, the dielectric constant will depend on the surface area of the particles, which in turn depends on the soil particle distribution. Hence, it can be concluded that soil texture, which is the percentage of clay, sand and silt, influences the dielectric constant. The dielectric constant is a function of frequency of the electromagnetic wave (f), physical temperature, volumetric soil moisture m_v, and soil texture [5]. The dielectric constant of dry soil is approximately 2 and around 20 for wet soil [5]. Given that the dielectric constant is a strong function of m_v, it is possible to estimate m_v by measuring the dielectric constant by distinguishing the intensities of the radar backscatter with a reasonable accuracy.

2.1.1 Sensitivity of soil moisture to microwave

Some of the issues that arise with respect to measurement of soil moisture using microwave are- Is there a significant change in backscatter with respect to change in dielectric constant? Can inversion models accurately determine even a slight change in dielectric constant in the presence of unavoidable calibration errors and errors obtained during determination of other depending parameters? These issues bring the sensitivity factor of both theoretical and empirical models.

2.2 DOBSON MODEL

The reference [5], investigates the dielectric behavior of soil medium with respect to soil texture, temperature and frequency. The experiments were performed at Lawrence, Kansas. The experimental fields were categorized as Fields 1-5, based on the soil texture. Two methods, wave-guide transmission technique and free-space transmission technique were employed in the measurement of dialectic constant of the categorized fields. From this experimental data set, *Dobson. et al.* established an empirical relationship between m_v from the observed ε and is given by:[5]

$$\varepsilon = (a_0 + a_1 S + a_2 C) + (b_0 + b_1 S + b_2 C) m_v + (c_0 + c_1 S + c_2 C) m_v^2 \tag{2.1}$$

where S, C is the volume fraction of sand and clay present in the soil. Volumetric soil moisture is preferred to gravimetric soil moisture because electromagnetic waves are a function of volume fraction of water present in the soil. This model takes into account the effects of soil texture, frequency, and temperature on the dielectric constant measurements and is based upon the work by *Dobson. et al.* [5].

2.2.1 Effects of soil texture

Soil moisture behavioral effects are different for the real $\varepsilon^{'}$ and imaginary $\varepsilon^{''}$ part of the dielectric constant. *Dobson. et al.* [5], found out that $\varepsilon^{'}$ is directly proportional to the sand content and inversely proportional to the clay content at any given frequency and soil moisture. This is evident in the polynomial curves in the plots (Figure 2.1). However, the sensitivity of $\varepsilon^{'}$ decreases, with an increase in frequency [5].

TABLE 1 COEFFICIENTS OF THE POLYNOMIAL EXPRESSION IN (2.1) [5]

Frequency	a_0	a_1	a_{21}	b_0	b_1	b_2	c_0	c_1	c_2
1.4	2.862	-0.012	0.001	3.803	0.462-	0.341	119.006	-0.500	0.6333
4	2.927	-0.012	-0.001	5.505	0.371	0.062	114.826	-0.389	-0.547
6	1.993	0.002	0.015	38.086	-0.176	-0.633	10.720	1.256	1.522

The coefficients of the polynomial in (2.1) are shown in Table 1 [5]. The soil texture effects can be studied by plotting the measured dielectric constant as a function of m_v for the fields with different textural composition. The behavior of m_v with respect to ε for different frequencies is illustrated in Figure 2.1. Field 1 is 51.5% volume fraction of sand and 13.5% volume fraction of clay and is designated *sandy loam*. Field 2 is 42.0% volume fraction of sand and 8.5% volume fraction of clay and is designated *loam*. Field 3 is 5% volume fraction of sand and 47.4% volume fraction of clay and is designated as *silty clay*. Soils that are rich in sand content have the least specific surface, and thus have a very low bound water volume fraction [5].

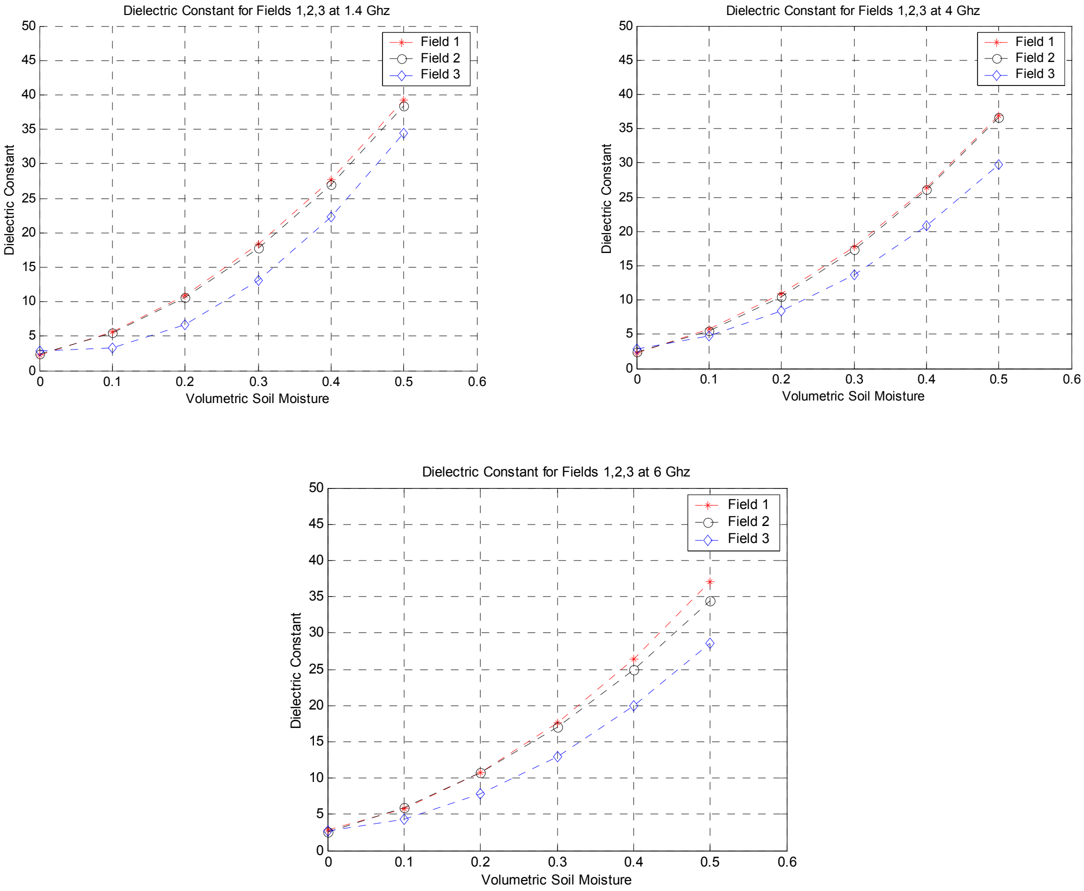

Figure 2.1 Dielectric constant as function of volumetric moisture for Fields 1, 2, 3 at 1.4, 4 and 6 GHz respectively

This is the reason why Field 1 exhibits a higher dielectric constant than other fields. From the plots, it is evident that the $\varepsilon^{'}$ exhibits similar behavior at all frequencies and is texture dependent. It is observed that the effects of texture reduce as frequency increases. The imaginary part of the dielectric constant is independent of soil texture at C band and is most sensitive to the volume fraction of clay at L band. This is because of the dominance of ionic conductivity due to the presence of liquid salts composed of calcium and that the calcium concentration increases with clay content [5].

2.2.2 Frequency & Temperature Effects

The real part of the dielectric constant decreases with increases in frequency and the imaginary part increases with increases in frequency for all the fields [5]. A decrease in temperature below the freezing point drastically reduces the dielectric constant due to the non-availability of free water [5].

2.3 SURFACE CHARACTERIZATION

From a statistical perspective, soil surfaces are generally expressed as *rms* height, correlation length and autocorrelation function. [6]. Determining these parameters or separating them from their contribution to the total backscatter (both experimentally and theoretically relating to backscatter) is perhaps the most challenging aspect in soil moisture estimation projects.

2.3.1 *rms* Height (h)

The root-mean-square (*rms*) surface roughness (known as *rms* height) describes the variation in surface elevation. It is an estimation of the variance of the vertical dimension in the test surface and is given by:

$$h = \sqrt{\frac{1}{N-1}\sum\left[h(p_n) - h(p)\right]^2} \tag{2.2}$$

where $h(p_n)$ is the height of the n^{th} horizontal position and $h(p)$ is the mean of the height and N is the number of samples.

2.3.2 Correlation Length (l)

Correlation length describes the similarity of the height over some distance along the surface. The maximum distance over which significant correlation occurs is known as correlation length. In other words, correlation length can be defined as the distance between two statistically independent points & for natural surfaces, as this distance increases, autocorrelation decreases. It gives a measure of the slope of the terrain. The correlation length is the value obtained when correlation function decreases by $1/e$. In Figure 2.2, the correlation length is 3 cm. When measuring l using a profilometer, the length of the profilometer should be at least greater than l [6].

2.3.3 Autocorrelation function

Some of the popular autocorrelation functions and their spectra are shown in Table 2 [19]. Theoretically, the exponential function best describes natural surfaces. From the observed measurements in [21], the rougher fields correspond to Gaussian correlation functions and smoother fields are better described by exponential functions.

TABLE 2 SOME AUTOCORRELATION FUNCTIONS AND THEIR SPECTRA

Autocorrelation Function	**Corresponding Spectrum ($W(-2k\sin\theta,0)$)**
Exponential, $\rho(\xi) = \exp(-\xi / L)$	$\left(\frac{L}{n}\right)^2 \left[1 + \left(\frac{KL}{n}\right)^2\right]^{-1..5}$
Gaussian, $\rho(\xi) = \exp(-\xi / L)^2$	$\left(\frac{L}{2n}\right)^2 \exp\left[-\left(\frac{KL}{4n}\right)^2\right]$
1.5 Power, $\rho(\xi) = (1 + \xi^2 / L^2)^{-1.5}$	$\frac{L^2 K^{1.5n-1} K_{-(1.5n-1)} K}{2^{1.5n-1}\Gamma(1.5n)}$

While mapping of the surface roughness profiles during the soil moisture experiments at Washita (*Washita'94*), the surface correlation function, $\rho(\xi) = \exp(-\xi / L)^n$ that best described the surface was when $n = 1$, for most cases. This value of n corresponds to exponential correlation function. This thesis assumes the exponential correlation function. The Fourier spectrum of the correlation functions is used in the soil moisture inversion algorithms (Figure 2.3). A separate (Neural Network) NN can be trained that determines the autocorrelation type for a given surface, but it demands multiple incident angle data.

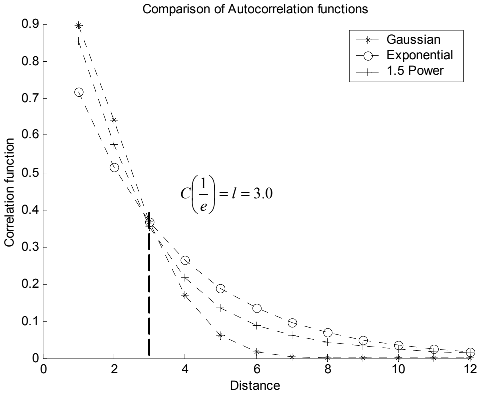

Figure 2.2 Comparison of Autocorrelation function

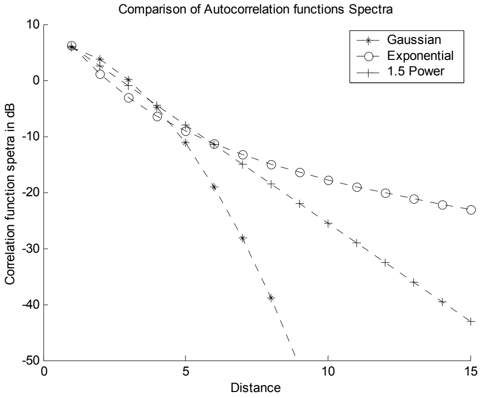

Figure 2.3 Fourier transform of the auto correlation function

2.4 SYNTHETIC APERTURE RADAR (SAR) OVERVIEW

Measurement of surface moisture from a traditional hydrological science perspective has been localized and largely relies on point measurements. Water has been recognized to play a fundamental role in Earth science. SAR plays an important role in Hydrology because of its high resolution, independency of the data time collection, immunity towards atmospheric attenuation, and its ability to see through the clouds. The development of SARs in the past two decades led to the transformation of hydrological engineering, from its focus on a regional scale, to a global scale. In the following paragraphs, some of parameters related to Radarsat are defined and the technical specifications of Radarsat are tabulated in Table 3 [10].

TABLE 3 RADARSAT TECHNICAL SPECIFICATIONS

Frequency	5 GHz, C band (5.6 cm)
Polarization	Horizontally transmit and receive (HH)
Resolution	8-100 m
Incident Angle	10°-60°
Repeat Cycle	24 days (Minimum – 3days)
Orbits per day	24
Beam Modes	Fine, Standard, Wide, Extended High & Low, ScanSar High & Low
Geometry	Sun-synchronous orbit
Altitude	798 km
Expected Life time	7 years

Orbits and Swaths: Orbits can generally be subdivided in to Geo-synchronous Earth Orbiting Satellite (GEOS), Low EOS (LEOS) and Medium EOS (MEOS). The space borne sensors usually have Sun synchronous orbit and are LEOS. The orbit path can be either ascending or descending passes. As a satellite revolves around the Earth, it illuminates an area on the Earth's plane. This illuminated area is known as the Swath. The path of the Satellite trajectory is known as the Azimuth and the point directly below the sensor is called the Nadir. Another term associated with swath is the Instantaneous Field of View (IFOW), which is defined as the angular cone of visibility. [8], [9].

Spatial Resolution: Spatial resolution is the size of the minimum possible feature that can be detected. The resolution cell is determined by the combination of Range Resolution and Azimuth resolution. Range is the minimum distance between two separate objects. Theoretically, spatial resolution is half the length of the transmitted Radar pulse. Azimuth resolution corresponds to the minimum distance between two objects in the direction of the azimuth. The beam width is directly proportional to the wavelength of the incident wave. Therefore, azimuth resolution is lower for higher wavelengths and can be increased by increasing the length of the antenna. It is impossible to place large antenna arrays in space. This problem is overcome by the method known as the Synthetic Aperture Radar (SAR) that "synthesizes" a very long antenna. Therefore, the distance traveled by the satellite is exploited to create a very large aperture antenna and the responses received by it are converted to image after intensive signal processing [8], [9].

Frequency of operation: SAR operates in the microwave region. Microwave waves occupy the frequency range of the electromagnetic spectrum as shown in Figure 2.4. Radarsat operates at 5.3 GHz.

Figure 2.4 Electromagnetic Spectrum of Microwave

Polarization: Polarization is defined with respect to the orientation of the electric field of the incident wave. The plane that is formed by the direction of the propagating incident wave and normal to the Earth's surface is known as the reference plane. If the electric field is in this plane then it is referred to as vertically polarized, but if the electric field is perpendicular to both the reference plane and normal, then it is referred to as a horizontally polarized wave [10]. Radarsat is capable of horizontally polarized transmission and reception.

Incident Angle: Incident angle is the angle between the planes of the direction of the propagating incident wave and the normal to the Earth's surface. The local incident angle is the angle where the incident wave strikes the Earth's surface (Figure 2.5). The interaction between the surface roughness and backscatter is a strong function of incident angle. For instance, the areas of similar roughness will appear brighter at the near end than at the far end of the SAR image. The changes in backscatter due to incident angle variation within an image pixel can be neglected. Since a SAR image covers a large distance, incident angle varies along the range direction and its effects have to be corrected.

Look direction: The *look direction* is the orientation of the incident wave to the alignment of features, such as row structures with respect to the transmitted radar signal. It also has an influence on the appearance of the SAR image. For example, agriculture crops planted in parallel rows appear differently when the viewed from different *look angles*. Generally, for agricultural terrains the local incident angle is replaced by the incident angle for such surfaces.[10].

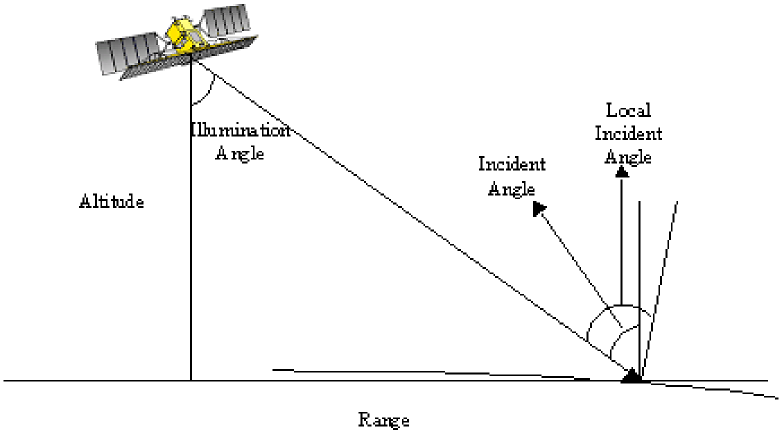

Figure 2.5 Radarsat angle descriptions

2.5 SURFACE SCATTERING

The degree of smoothness is defined in terms of the Radar wavelength. The models described in future sections normalize the roughness parameter. Those surfaces that are relatively smooth like calm water and roadways reflect the incident wave opposite to the direction of the sensor, thus appearing dark in a SAR image. These are also called specular surfaces. As the roughness increases, the amount of backscatter increases and this is called diffused reflectance.

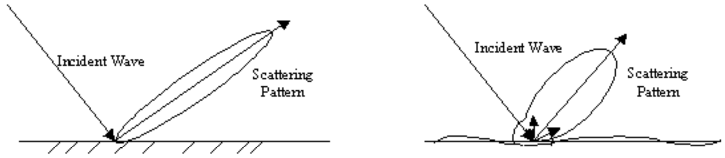

(a) Specular Reflection (b) Medium Scattering

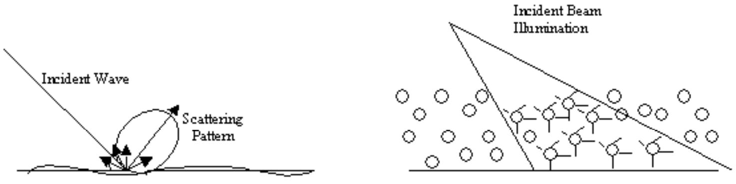

(c) Rough Scattering (d) Volume Scattering

Figure 2. 6Different scattering mechanisms [16]

There are two type of scattering: surface scattering and volume scattering. Surface scattering are single scattering terms as a result of the incident wave impinging on the surface that is moderately rough and may also arise due to outer canopy scattering. When an electromagnetic wave hits the boundary between two semi-infinite media, a part is reflected and the rest is transmitted to the medium. If the medium is a homogeneous mixture and is considered smooth, then the backscatter is very less and is considered only to as a surface scattering problem. As the medium becomes rougher, backscatter increases. Volume scattering may arise when the incident wave penetrates the surface, (usually when dry) and due to vegetation canopies because multiple scattering occurs within the medium. These types of scattering are depicted in Figure 2.6 [16].

The IEM model described in this thesis is for surface scattering and hence the multiple scattering terms have to be eliminated. The multiple scattering terms can be removed from fully parametric Radar data using the Cloude’s target decomposition algorithm [11]. Since Radarsat data is not fully parametric, this algorithm cannot be applied on Radarsat data. These terms have to be removed with the aid of visible/ infrared imagery.

CHAPTER III

DATA SYNOPSIS

This chapter summarizes two major test sites and field experiments that were conducted as part of the soil moisture campaign, namely the Soil Moisture Experiments, 2002 (*Smex02*) experiment and the *Washita'94* experiment.

3.1 *WASHITA'94* EXPERIMENT

Washita'94 experiment was a large-scale hydrological field campaign conducted over Little Watershed River watershed, Chickasha, Oklahoma. The experiment was conducted jointly by NASA, USDA, and Princeton University. The main objective of the campaign was to provide remotely sensed data and ground measurements for analysis of variables that contribute to the hydrological cycle [12].

3.1.1 Satellite Data

The *Washita'94* experiment was conducted during April 11-17, 1994 so that it coincided with Shuttle Imaging Radar & C- Band/ X band SAR (SIR-C/X-SAR) mission. SIR-C provided images at L, C and X bands with the following polarization combinations :HH,HV,VV. The incident angles and the polarization combinations of some of the images that were used to derive soil moisture maps are shown inTable 4. Multi-spectral imagery was provided by Landsat TM. The images were acquired on April 12, 1994 with a resolution of 30m.

TABLE 4 RADARSAT & SIR-C DATA COVERAGE [7]

Date & UTC Time	Look angle &A/D* modes	Incident angle at center	Pixel Spacing	Latitude &Longitude	
June 14, 2002	34.15 D	41.48	50.00	43.61	-92.29
June 14, 2002	29.52 A	33.48	12.5	41.99	-93.20
June 24, 2002	40.26 A	46.46	12.5	42.38	-93.30
June 24, 2002	20.38 D	22.88	12.5	41.93	-93.26
June 28, 2002	23.82 A	26.84	12.5	41.99	-93.44
June 28, 2003	38.21 D	43.91	12.50	41.93	-93.44
July 1, 2002	34.15 A	41.48	50.00	41.59	-93.95
July 8, 2002	34.15 D	41.48	50.00	42.36	-94.37
July 18, 2002	40.23 D	46.42	12.5	41.99	-93.31
July 18, 2002	20.38 D	22.88	12.5	41.94	-93.26
July 22, 2002	23.82 A	26.84	12.5	41.98	-93.43
July 22, 2003	38.21 D	43.92	12.5	41.92	-93.43

SIR-C

Date	A/ D modes	Incident angle at center	Resolution	Polarization	Processing+
April 11, 1994	A	28.0	30	HH, HV, VV	slc
April 12, 1994	A	42.3	30	HH, HV, VV	slc
April 13, 1994	A	50.1	30	HH, HV, VV	slc
April 15, 1994	A	56.3	30	HH, HV, VV	mlc

*Ascending/Descending

+File Formats slc: Single look Complex, mlc: Multi-look Complex

3.1.2 Site Characterstics

A number of surface measurements were sampled from various locations to fit with a general correlation function [13]:

$$\rho(\xi) = \exp(-(\xi / l)^n) \tag{3.1}$$

It is found that exponential function ($n = 1$), provided the best fit followed by when $n = 1.4$. Therefore, during the development of the SM (Shi Model (SM)), the correlation functions with $n \leq 1.4$ are chosen for IEM simulations [13].

The sites were categorized based on the characteristics that describe the region and are shown in Table 5.

TABLE 5 PARAMETERS MEASURED DURING WASHITA '94 SITE CHARACTERIZATION

Land Cover	Bulk Density	Vegetation Biomass			Surface Roughness	
		Dry Biomass	Wet Biomass	Vegetation Water content	*rms* height	Correlation length

3.1.3 Methods for measuring soil roughness

Laser Profilometer: The system consists of a laser measurement unit mounted on an automated (x, y) positioning table. The table is placed at a height of 1.5 m from the surface (x, y) to be measured. The vertical distance from the table to the point is measured. The position of the laser on the x, y plane can be accurately controlled and the linear and complete surface profile can be mapped [7].

Paint and paper profiler: A graph paper is wrapped around a thin metal sheet and inserted in to the surface such that the horizontal plane is in level. Black paint is sprayed so that the surface profile is imprinted on the graph paper. The vertical distance from the paint line is recorded at uniform horizontal positions thus transforming to numerical data. By using a long sheet, a continuous surface profile can be recorded [7]

Figure 3.1 Laser Profilometer [7]

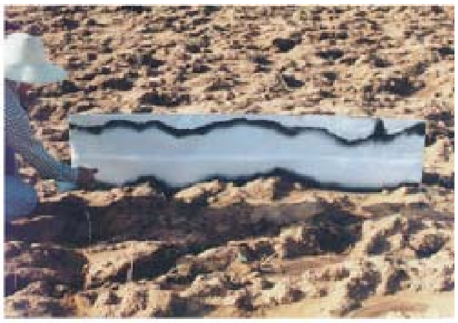

Figure 3.2 Paint & Paper Method [7]

3.1.4 Measuring Soil moisture

Gravimetric soil moisture is obtained from samples that were obtained from different sites of the experimental area. The volumetric soil moisture is calculated by multiplying gravimetric soil moisture by the soil bulk density. The volumetric soil moisture was also obtained using Time Domain Reflectometry instrument. The experiments plan and site characteristics are described in detail in [12] & [14].

3.2 SMEXO2

The key objective of the *Smex02* is to develop soil moisture products from data provided by satellite platforms that include radiometers, (AMSR), radar (Radarsat, ERS-2, Quicksat) and visible/infrared observations (Landsat, NOAA AVHRR). The*Smex02* were conducted in the months of June & July, 2002 over Walnut Creek (WC) watershed, south of Ames, Iowa [15].

3.2.1 Land Cover

Agriculture crops, Soybean and Corn cover the study region by 95% and the remaining percentage being forage and grains [15]. Soil types vary a lot within the region. Vegetation characteristics such as plant height, LAI, green and dry biomass were sampled throughout the WC sites.

3.2.2 Measurement of Surface Parameters

Three types of sampling are made for measuring volumetric soil moisture, which are Watershed sampling, Regional sampling, Tower sampling. Watershed sampling, and Regional sampling are made with an objective of providing validation for soil moisture inversion algorithms derived from aircraft and satellite platforms respectively. Volumetric soil moisture is calculated by converting dielectric constant measured using a theta probe at a depth of 0-6 cm. The paint & paper profile method was used in *Washita'94* experiment is used for measuring surface roughness. The *Smex02* surface parameters data are not released for performing analysis & validation.

3.2.3 Satellite Data

Landsat 5 & 7 were employed to provide multi-temporal coverage in the visible/infrared bands. Landsat data can provide valuable data such as vegetation water content maps, vegetation classification maps, and LAI for soil moisture estimation.

The temporal coverage of Radarsat data is provided in Table 4 along with date, incident angle, pixel spacing and look angle details. The Radarsat data format depends on the facility that converts the raw SAR data to images that can be used for analysis. The Radarsat beam modes that are best suited for soil moisture are fine & standard modes. The fine and the standard modes have a resolution of 8 m and 25 m respectively. All the Radarsat images are in ASF (Alaska SAR Facility) format. The Radarsat data have to be first calibrated and removed of speckle noise. The reflected Radar may experience random fluctuations or fading resulting in brighter or darker pixels than the mean associated with the backscatter. One method of removing the “speckle” from the input image is by removing the high frequency components by a 3x3 or 5x5 low pass filter. Then the image is geocoded so that it includes all the WC sites and has the resolution of Landsat image (30 m).

Two images acquired by Radarsat that are calibrated and geocoded are shown in Figure 3.3. The images are acquired at an incident angle of 41.48 (at the center of the image) on June 27 & July 20.

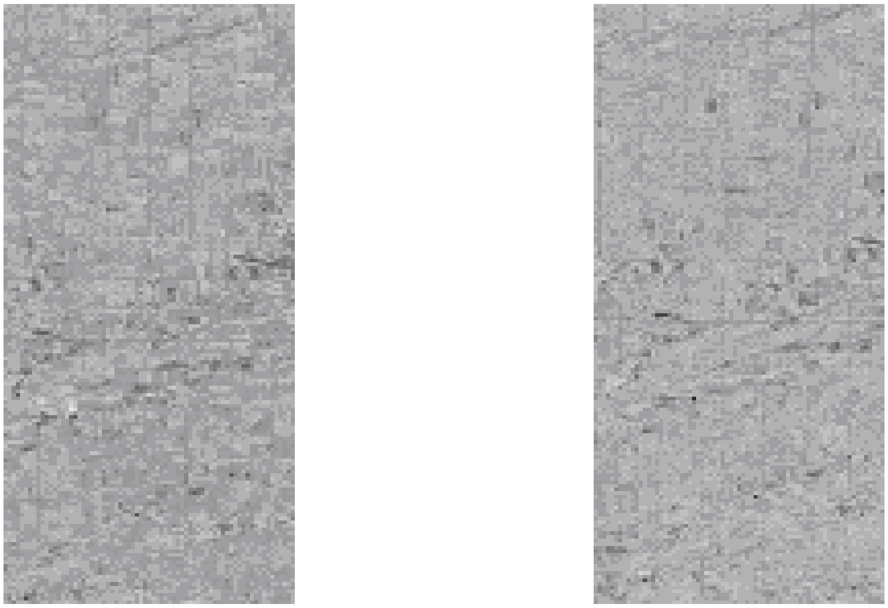

Figure 3.3 Geocoded and Calibrated Radarsat images of Walnut Creek, Iowa on June 27 & July 20

CHAPTER IV

CURRENT KNOWLEDGE & METHODS

Scattering models for isotropically random surfaces (soil surfaces) can be categorized into theoretical and empirical models. This chapter gives a quantitative comparison of the theoretical and existing empirical models and briefly discusses the results obtained through them.

4.1 THEORETICAL MODELS

Theoretical models are classified based on the region of their validity, and region refers to surface roughness. The next sections compare these models within their validity against IEM model, because of unavailability of actual data.

4.1.1 Physical Optics Model (PO, Relatively smooth surface)

Generally, the backscatter coefficient received (4.1), consists of coherent and non-coherent terms. Coherent term has a major contribution at near normal incidence and the non-coherent term is important at all the angles [16].

$$\sigma_{pp}^{0}(\theta) = \sigma_{ppc}^{0}(\theta) + \sigma_{ppn}^{0} \tag{4.1}$$

where p denotes the polarization type. The coherent term is developed by *Fung*. and *Eom*. and is given by [16]:

$$\sigma_{ppc}^{0}(\theta) \cong \frac{\Gamma_p(\theta)}{B^2}\exp\left(-4k^2\sigma^2\right)\exp\left(-\theta^2 / B^2\right) \tag{4.2}$$

where $B^2 = (KR_0\beta)^{-2} + (\beta/2)^2$, $\Gamma_p(\theta)$ is the reflection coefficient, θ is the incident angle, $k = 2\pi/\lambda$, σ is the surface *rms* height, R_0 is the range of the antenna to the center of illumination and β is the one sided beam width of the antenna. The non-coherent term can be expressed as [16]:

$$\begin{aligned}&\sigma^0_{ppn}(\theta) = 2k^2\cos^2\theta\Gamma_p(\theta)\exp[-(2k\cos\theta)^2]\cdot\\&\sum_{n=1}^{\infty}[(4k^2\sigma^2\cos^2\theta)^n/n!]\cdot\\&\int_0^{\infty}\rho^n(\xi)J_0(2k\xi\sin\theta)\xi d\xi\end{aligned} \tag{4.3}$$

where σ is the *rms* height and J_0 is the zero order Bessel function of the first kind and $\rho(\xi)$ is the surface correlation function. The model is referred to as *Kirchhoff model under scalar approximation or physical optics model* [16]. The model is valid only for bistatic cases or specular surfaces.

TABLE 6 VALIDITY CONDITION FOR THEORETICAL MODELS [16]

Theoretical model	**Validity range**
Physical optics	$m < 0.25$, $kl > 6$ and $l^2 > 2.76\sigma\lambda$
Geometric optics	$(2k\sigma\cos\theta)^2 > 10$ and $l^2 > 2.76\sigma\lambda$
Small Perturbation Model	$k\sigma < 0.3$, $m < 0.3$

4.1.2 Geometric Optics Model (GO, Relatively Rough Surfaces)

For relatively rough surface the geometric model or otherwise known as *Kirchhoff model under stationary phase approximation,* is used [16]:

$$\sigma^0_{ppn}(\theta) = \frac{\Gamma(0)\exp(-\tan^2\theta/2m^2)}{2m^2\cos^4\theta} \tag{4.4}$$

where m is the *rms* slope and $\Gamma(0)$ is the Fresnel reflectivity at normal incidence. The non-coherent term is dominant for rough surfaces and the coherent term can be neglected. From Figure 4.1, as *rms* height increases the slope of the backscatter curve decreases.

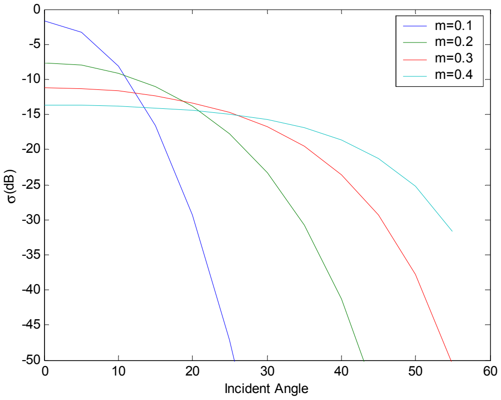

Figure 4.1 GO model simulations for varying *rms* slopes

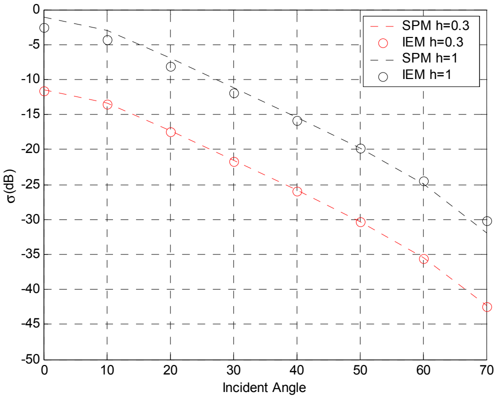

Figure 4.2 Angular trend of IEM and SPM models, (l=5, $\varepsilon = 20$)

4.1.3 Small Perturbation Model (SPM, For slightly rough surface)

The backscattering coefficient is given by [16]:

$$\sigma^0_{ppn}(\theta) = 8k^4\sigma^2\cos^4\theta\left|\alpha_{pp}(\theta)\right|^2 W(2k\sin\theta) \qquad (4.5)$$

where W is the normalized roughness spectrum and $\alpha_{pp}(\theta)$ is the polarization amplitude. The expressions given above show a direct relationship between the backscatter coefficient and the reflection coefficient. The SPM is valid for regions with $kl < 6$. From the plots above, IEM and SPM are in excellent agreement. Theoretically, IEM reduces to an expression "similar" to SPM (4.5) for small *rms* height [17]. The correlation degrades as *rms* height increases (Figure 4.2). The regions of validity for all the three theoretical models are tabulated in Table 6.

4.1.4 Integral Equation Method (IEM)

According to *Fung. et al.* [17], "*The IEM is a backscattering model for scattering from a randomly rough dielectric surface that is based on an approximate solution of a pair of integral equations for the tangential surface fields*". The IEM model for HH polarization contains two types of coefficients, single and multiple scattering terms and contributions due to single scattering terms are dominant in the case of small and medium dielectric surfaces. Therefore, the multiple scattering terms can be ignored. The model described below is suitable for dielectric surfaces with small and medium roughness ($kh < 3$) [17]. Detailed derivation of the IEM model is dealt in [17] and is beyond the scope of this thesis. The following are the results of special cases of the final derived result in [17].

Soil surface is treated as an inhomogeneous rough surface and the backscatter coefficient for HH polarization is given by [17]:

$$\sigma_{hh} = \frac{k^2}{2}\exp(-2k_z^2h^2)\sum_{n=1}^{\infty}\left|I_{hh}^n\right|^2 \frac{W^{(n)}(-2k_x,0)}{n!} \tag{4.6}$$

where $k_Z = k\cos\theta, k_x = k\sin\theta$ and θ is the incident angle.

$$I_{hh}^n = (2k_Z\sigma)^n f_{hh}\exp(-k_Z^2\sigma^2) + \frac{(k_Z\sigma)^n\left[F_{hh}(-k_x,0)+F_{hh}(k_x,0)\right]}{2} \tag{4.7}$$

$$f_{hh} = 2R_{\perp}/\cos\theta \tag{4.8}$$

$$F_{hh}(-k_x,0)+F_{hh}(-k_x,0) = \left[\left(1-\frac{1}{\mu_r}\right)+\frac{\mu_r\varepsilon_r-\sin^2\theta-\mu_r\cos^2\theta}{\mu_r^2\cos^2\theta}\right] \tag{4.9}$$

$R_{\perp}$, is the Fresnel reflection coefficient for horizontal polarization and is given by

$$R_{\perp}=\frac{\cos\theta-\sqrt{\varepsilon_r-\sin^2\theta}}{\cos\theta+\sqrt{\varepsilon_r-\sin^2\theta}} \tag{4.10}$$

$R_{\perp}$ reduces to 1, for perfectly conducting surfaces. The local incident angle in the relation (4.10) can be replaced by incident angle. $W^{(n)}(K)$ is defined as the Fourier transform of the n^{th} power of the correlation function [13]. Exponential and Gaussian are the popular types of correlation functions used. Exponential correlation functions describe smooth natural surfaces while Gaussian correlation functions correlate well with rough surfaces [21]. The Fourier transform of the n^{th} power of a correlation function is given by [13]:

$$W^{(n)}(K)=\int_{0}^{\infty}\rho^{n}(\xi)J_0(K\xi)d\xi \tag{4.11}$$

where J_0 is the Bessel function of first kind, $K=2k\sin\theta$ for backscatter from a dielectric surface. The behavior of the backscatter can be studied by simulation of the IEM model, for different variable parameters. The main parameters h,l,ε are varied and the backscatter is plotted against the incident angle for HH polarization below.

4.1.4.1 *Behavior of* h

It is evident from Figure 4.3 that as h increases, backscatter increases. It can be observed that the change in backscatter widens with increase in incident angle. Therefore, at lower incident angles the effect of h is negligible. This conclusion can also be made from Figure 4.4. The plot also shows that the backscatter at lower incident angle reaches saturation faster than at a higher incident angle. Multiple scattering terms tend to dominate single scattering as frequency of the incident wave increases or with an increase in h.

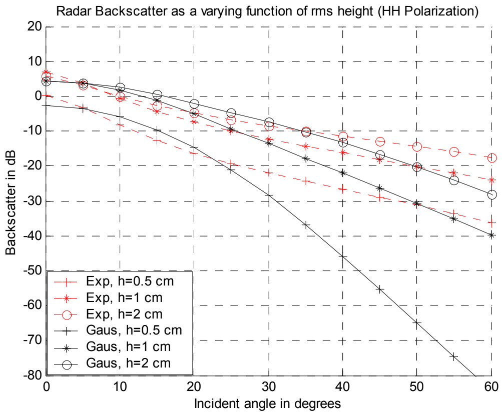

Figure 4.3 Radar backscatter as a function of h, $\varepsilon = 10, l = 10$

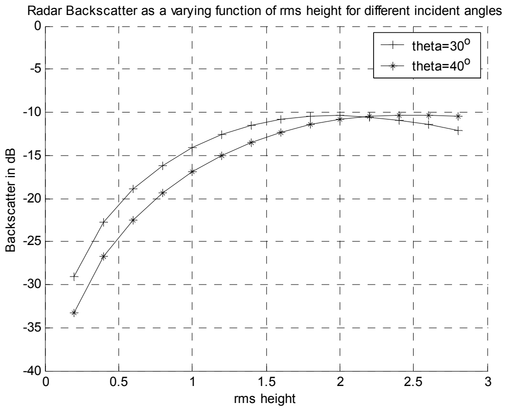

Figure 4.4 Effect of *rms* height on Backscatter, $l = 15$ cm, $\varepsilon = 3$, C band

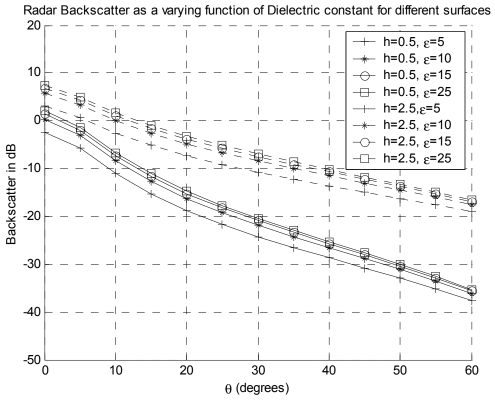

Figure 4.5 Backscatter as a function of ε, for different surfaces, $l = 15$ cm

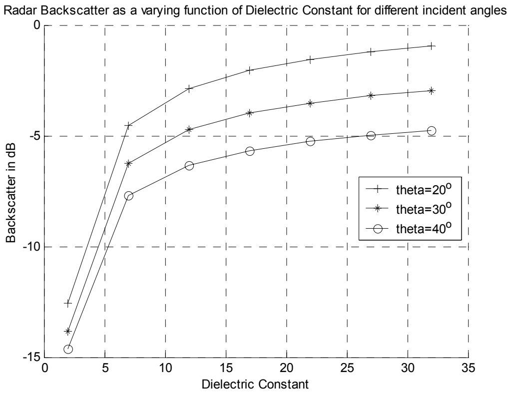

Figure 4.6 Backscatter as a function of dielectric constant for various incidence angles, $h = 2$ cm, $l = 20$ cm**, Frequency=5 GHz.**

4.1.4.2 *Behavior of ε*

With the help of Figure 4.5, and Figure 4.6, the behavior of dielectric constant can be explained. Backscatter increases with increase in dielectric constant, but the increase reaches a saturation when $\varepsilon > 30$. Another important observation is that the change in ε only changes the level of the backscatter curve, but change in l, h changes the level and shape of the curve. This was also pointed out by *Fung. et al.* [18], and is an important feature in the training data set for the back propagation model. A change in value of $\sigma_{hh} \approx 10.5\,\mathrm{dB}$ is observed when dielectric constant is changed from 2 (dry soil) to 25 (wet soil) at $\theta = 30^\circ$.

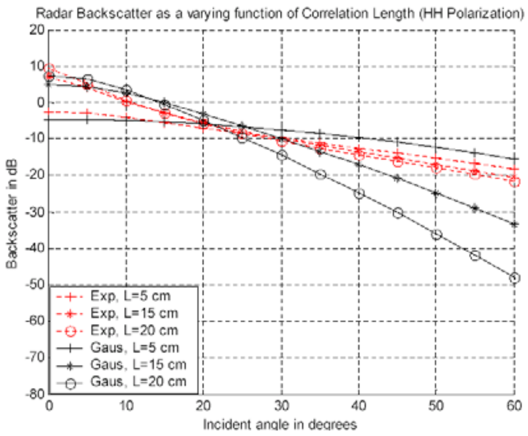

Figure 4.7 Backscatter as a function of l, $h = 1\,\mathrm{cm}, \varepsilon = 10$

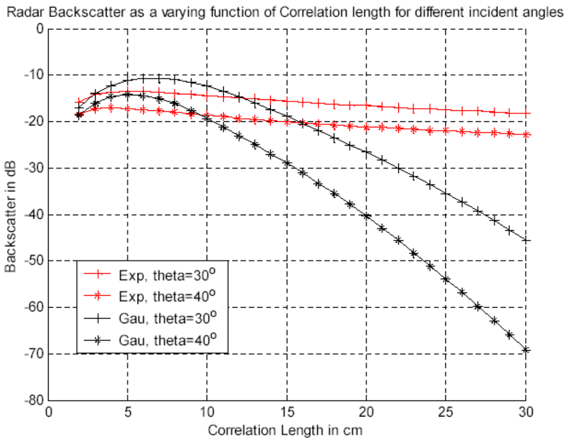

Figure 4.8 Effect of correlation length on backscatter, $\varepsilon = 10$, L band, $h = 1\,\mathrm{cm}$

4.1.4.3 *Effect of correlation length*

The effect of correlation length on backscatter is much greater at Gaussian correlation than at exponential correlation (Figure 4.8). As correlation length increases, backscatter drops of faster (Figure 4.7). Generally, backscatter values, as a function of exponential correlation, is much higher than Gaussian correlation at larger incident angles. Natural surfaces correlate well with exponential correlation function at lower incident angles and for slightly rough surfaces [19].

4.1.4.4 *Transition model*

The Fresnel reflection terms are evaluated at either incident angle or specular angle. These two options lead to an ambiguity as to what angle is suitable for different surfaces. There is also an uncertainty regarding the cases (h,l) that fall in the middle category [20]. This may cause a sudden transition in the backscatter. To compensate for these effects a transition model was derived and the Fresnel reflection coefficients modified [20]:

$$R_h(T) = R_h(\theta_i) + \left[R_h(0) - R_h(\theta_i)\right]\gamma_h \tag{4.12}$$

where $R_h(T)$ is the *modified* reflection coefficient, $R_h(\theta_i)$ and $R_h(0)$ is the reflection coefficient evaluated incident angle and specular angle respectively. The transition function for HH polarization is given as [20]:

$$\gamma_h = 1 - S_{hh} / S_{hh}^0 \tag{4.13}$$

where:

$$S_{hh} = \frac{\frac{1}{4}\sum_{n=1}^{\infty} \frac{(k\sigma\cos\theta_i)^{2n}}{n!} \left|F_h\right|^2 W^{(n)}(-2k_x,0)}{\sum_{n=1}^{\infty} \frac{(k\sigma\cos\theta_i)^{2n}}{n!} \left|2^{n+1}\frac{R_h(0)}{\cos\theta_i}\exp\left[-(k\sigma\cos\theta_i)^2\right] + \frac{F_h}{2}\right|^2 \left(W^{(n)} - 2k_x,0\right)} \tag{4.14}$$

and $$F_h = -8R_h^2(0)\sin^2\theta_i \left(\frac{\cos\theta_i + \sqrt{\varepsilon_r - \sin^2\theta_i}}{\sqrt{\varepsilon_r - \sin^2\theta_i}\,\cos\theta_i}\right) \tag{4.15}$$

The term S_{hh}^0 is calculated by letting n of 4.14 to 1, *i.e.* $k\sigma$ is close to unity. γ_h has values between 0 and 1. For relatively smooth surfaces ($k\sigma$~0), γ_h approaches 0 and $R_h(T) \to R_h(\theta_i)$ and $R_h(T) \to R_h(0)$ for rough surfaces [20]. Similarly, in the low frequency region, $R_h(T) = R_h(\theta_i)$, and $R_h(T) = R_h(0)$ in the high frequency region. The behavior of the transition coefficient is illustrated in Figure 4.9, Figure 4.10, & Figure 4.11.

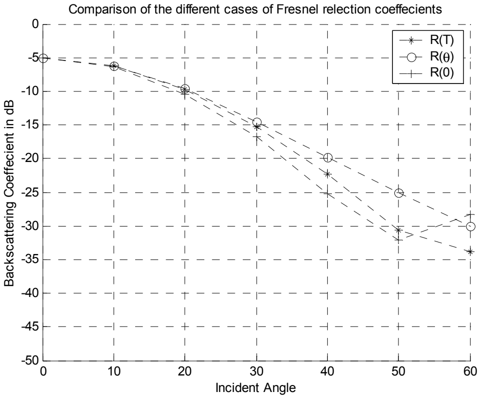

Figure 4.9 Comparison of different cases of Fresnel reflection coefficients, Gaussian correlation function, $h = 1.42\,\text{cm}, l = 10\,\text{cm}$

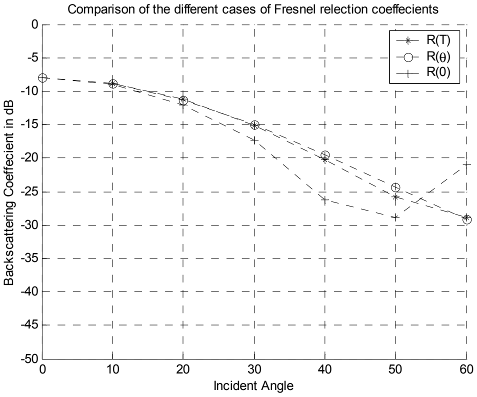

Figure 4.10 Comparison of different cases of Fresnel reflection coefficients for Gaussian correlation function, at $h = 1.14\,\text{cm}, l = 8\,\text{cm}$

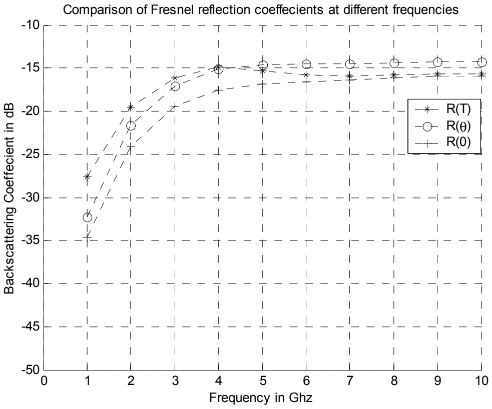

Figure 4.11 Frequency trends of backscatter for Fresnel reflection coefficients for $h = 0.42\,\text{cm}, l = 3.0\,\text{cm}$

At small incident angles, there is not much difference in the behavior of the backscatter for all three cases of the reflection coefficients. The new model was verified using a moment method simulation [20]. The transition model can be applied to surfaces having Gaussian and 1.5 power correlation functions [20].

4.2 EMPIRICAL MODELS

Theoretical models like the SPM, GO and the PO models mentioned in the previous section predict soil moisture well but cannot be applied to natural surfaces because the ground parameters obtained from these surfaces fall outside the validity of these models. To overcome these limitations, empirical models are derived and are discussed in the following sections [21], [1]. Dielectric constant is a difficult parameter to measure, because Radar backscatter will depend on too many unknown parameters, namely correlation length, *rms* height, correlation function, and soil texture.

It is necessary to have data takes at multi-polarizations, multi-frequency or multi-incident angles to derive these parameters. *Tsan. et al.* [22] derived a simple model to derive these parameters using dual frequency. *Oh. et al.*, *Dubois. et al.*, and *Shi. et al.* derived soil moisture algorithms from multi-polarized data and is discussed in detail. The OH, Dubois, and Shi models (From the first authors of the respective models) are the most popular and referred empirical soil moisture inversion models. These algorithms were applied to SIR-C (Shuttle Imaging Radar) measurements at L band during the *Washita'94* experiment and their results are discussed.

4.2.1 OH Model

An empirical inversion algorithm is determined from parametric radar measurements that are obtained from ground-based scatterometers. The University of Michigan's LCX POLARSCAT (truck based scatterometers) obtained radar backscatter at frequencies 1.25(L), 4.75(C) GHz and 9.5(X) GHz at incident angles ranging from 10^o to 70^o [21]. Four different surfaces namely S1, S2, S3, S4 are chosen for study. The surface dielectric constant of these surfaces is measured using a field portable probe that operates at C band. The surface characteristics and experimental observations are shown in Table 7 [21].

TABLE 7 OH MODEL EXPERIMENTAL RESULTS

Surface	*rms height(cm)*	*Correlation Length(cm)*	*Measured surface ε (4.8 GHz)*		*Calculated surface ε (4.75 GHz)*	
			Wet	Dry	Wet	Dry
S1	0.40	8.4	14.15	6.58	15.42	8.77
S2	0.32	9.9	14.66	4.87	14.47	6.66
S3	1.12	8.4	15.20	7.04	15.23	8.50
S4	3.02	8.8	8.80	7.28	9.64	8.04

The autocorrelation of these surfaces are found to be exponential for smooth surfaces and Gaussian for rough surfaces. Soil moisture at a depth of 4 cm is also observed for wet and dry surfaces

4.2.1.1 *OH model characteristics*

The behavior of the observed measurements would be similar to the derived model. Therefore the model simulations are used here for discussing the analysis and would be compared with IEM model (Figure 4.12, Figure 4.13).

Cross-polarized ratios $q = \sigma_{hv} / \sigma_{vv}$ and co-polarized ratios $p = \sigma_{hh} / \sigma_{vv}$ are calculated from the observations obtained by the scatterometer, as a function of normalized surface roughness kh. An empirical function is determined that provided the best fit for the observed data and is given by [21]:

$$q = \frac{\sigma_{hv}}{\sigma_{vv}} = 0.23\sqrt{\Gamma}\left[1 - \exp(-kh)\right] \qquad (4.16)$$

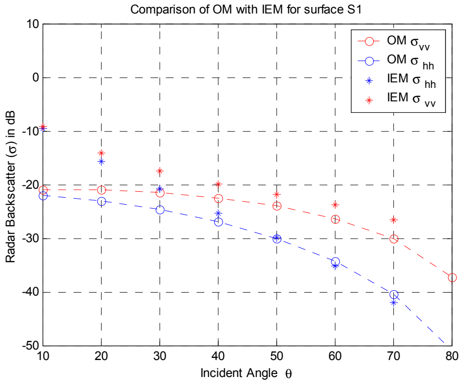

Figure 4.12 Angular comparisons of IEM and OH model for surface S1 (h =0.4 and l =8.4 at L band)

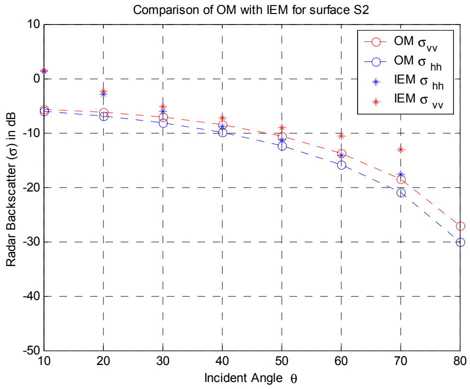

Figure 4.13 Angular comparisons of IEM and OH model for surface S2 (h =1.1 and l =8.4 at C band)

where Γ is the Fresnel reflectivity at incident angle $=90^o$:

$$\Gamma = \left| \frac{1-\sqrt{\varepsilon_r}}{1+\sqrt{\varepsilon_r}} \right| \tag{4.17}$$

Similarly the co-polarized ratio is given by [21]:

$$\sqrt{p} = \sqrt{\frac{\sigma_{hh}}{\sigma_{vv}}} = 1 - \left(\frac{2\theta}{\pi} \right)^{[1/3\Gamma]} \exp(-kh) \tag{4.18}$$

The next task is to determine the horizontal and vertical backscattering coefficients as a function of surface parameters from the observed data and the backscattering coefficients are obtained as [21]:

$$\sigma_{vv}(\theta, \varepsilon_r, kh) = \frac{g\cos^3\theta}{\sqrt{p}} [\Gamma_v(\theta) + \Gamma_h(\theta)] \tag{4.19}$$

where $g = 0.7\left[1 - \exp(-0.65(kh)^{1.8})\right]$ (4.20)

and $\sigma_{hh}(\theta, \varepsilon_r, kh) = g\sqrt{p}\cos^3\theta[\Gamma_v(\theta) + \Gamma_h(\theta)]$ (4.21)

σ_{hh} and σ_{vv} are proportional to the average of horizontal and vertical Fresnel reflection coefficients [21]. The difference between σ_{hh} and σ_{vv} increases with increase in incident angle and decreases with increase in soil roughness (Figures above) [21]. The functions p and q of 4.16 and 4.18 are plotted in Figure 4.14, and Figure 4.15 respectively. The ratio $p > 1$ is in agreement with Radar observations and theoretical models. This ratio increases with surface roughness and becomes independent of incident angle [21].

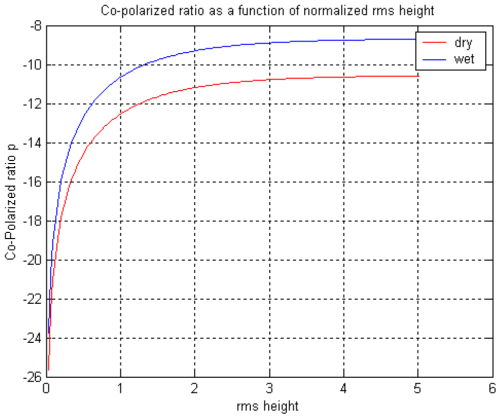

Figure 4.14 Co-polarized ratio as a function of *rms* height at 40º

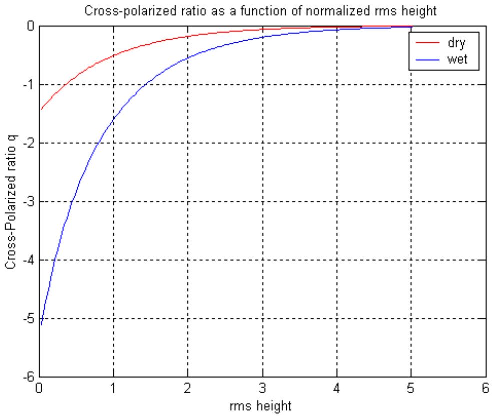

Figure 4.15 Cross-polarized ratio as a function of *rms* height at 40º

4.2.1.2 *Conclusions*

The OH model requires the knowledge of cross-polarized backscatter ratio and its behavior is quite different from co-polarized ratio. The region of validity of this model is given as $2.5 \le kl \le 20$, and $0.09 \le m_v \le 0.31$. OH model is one of the first empirical models that inverted m_v using multi-polarized radar observations with an *rmse* of 0.04 when compared to ground results [21]. OH model did not provide promising results when applied to SAR data [23].

4.2.2 Dubois Model (DM)

Similar to the OH model discussed in the previous section, *Dubois. et al.*, developed an empirical model from the data set obtained from a wide range of surfaces using LCX POLARSCAT & RASAM scatterometers. The RASAM is also a truck-based scatterometer, and is capable of observing both co-polarized and cross-polarized backscatter over the incident angle range 30º-60º. This algorithm is developed to determine soil moisture from multi-polarized data. The algorithm is developed for $\theta > 30^o, kh < 2.5\,\text{cm}\,\&\, m_v < 35\%$. The *rms* error in the estimated soil moisture using DM is found to be less than 4.2 % [1].

4.2.2.1 *Experimental data set*

The data set acquired using LCX POLARSCAT scatterometer is discussed in the previous section. The second set of data is obtained using RASAM scatterometer-radiometer. The RASAM data set included hh, vv, hv, vh polarized backscattering coefficients taken at incident angles in the range $30^o - 60^o$. Only those coefficients backscattered from bare soil surface pixels are considered for the data set. The surface profiles are mapped using a laser profilometer [24].

The relationship between the backscattering coefficients and dielectric constant, *rms* height and incident angle is derived as follows. LCX POLARSCAT was used to measure backscatter coefficients of the same pixel at two different moisture conditions for different surfaces (Table 7). The RASAM scatterometer operates at frequencies in the range of 2.5-11 GHz. The scatterometers covered surfaces ranging from 0.57-1.12 cm. From these measurements, the coefficient multiplying $\varepsilon \tan\theta$ is calculated. The backscatter at VV and HH polarizations, derived from the above-mentioned data set is given by [1]:

$$\sigma_{hh}^{0} = 10^{-2.75}\frac{\cos^{1.5}\theta}{\sin\theta^{5}}10^{0.028\varepsilon\tan\theta}(kh\sin^{1.4}\theta)\lambda^{0.7} \tag{4.22}$$

$$\sigma_{vv}^{0} = 10^{-2.35}\frac{\cos^{3}\theta}{\sin\theta}10^{0.046\varepsilon\tan\theta}(kh\sin^{3}\theta)^{1.1}\lambda^{0.7} \tag{4.23}$$

where σ_{hh}, σ_{vv} are the backscattering coefficients, θ is the incident angle, kh is the normalized *rms* height with respect to a frequency of 1.5 GHz, λ is the wavelength of the incident wave.

As mentioned in the previous section, the backscatter using the POLARSCAT scatterometer is measured at incident angles with intervals of 10^{o} in the range $10^{o} - 70^{o}$. It is observed that the angular behavior follows a tangential behavior [1]. The roughness characteristics are found from the measurements obtained by both the scatterometers, by dividing with ε, θ [1]. The parameter $kh\sin\theta$ is treated as a dimensionless quantity of the projected *rms* height on the *incident* wave plane [1]. This model predicts $\sigma_{hh} > \sigma_{vv}$ which is contradictory to GO & IEM model predictions and the observed SAR data [1]. To ensure this validity, the DM is restricted to $kh \leq 2.5$ cm and to $\theta > 30^{o}$. Most of the natural surfaces fall within this range. The backscatter obtained, from the relation developed by *Dubois. et al.* [1] do not follow the SPM. It is reasoned out in [1] that the ratio σ_{hh}/σ_{vv} increases with increase in roughness because of the difference in power, but SPM predicts that the ratio does not increase with increase in roughness. Figure 4.16, shows not much correlation between DM and SPM & IEM models for very smooth surfaces ($h = 0.2\,\text{cm}$) for a wide range of incident angles. IEM model and DM correlate well in the incident angle range 30°-70°(Figure 4.17).

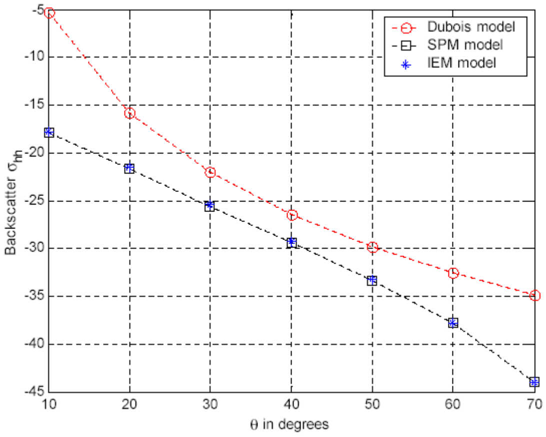

Figure 4.16 Angular trend comparison of Dubois model with SPM and IEM for h =0.2 cm, l =5 cm

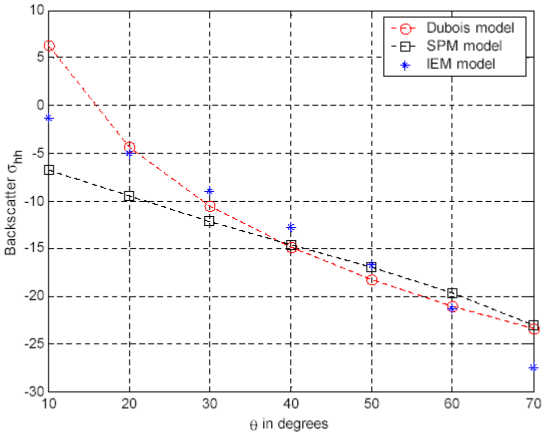

Figure 4.17 Angular trend comparison of Dubois model with SPM and IEM for h =2 cm, l =5 cm

One of the main advantages of DM over OH model, is that the dielectric constant can be calculated by eliminating *rms* height from co-polarized data rather than from cross-polarized data because co-polarized data channels can be calibrated with passive targets and cross-polarized channels are calibrated using co-polarized channels, thus less accurate [1]. One other factor is that co-polarized channels are more sensitive to vegetation. After eliminating the *rms* height using 4.22 and 4.23, ε can be written in terms of backscatter acquired through horizontal and vertical polarizations [1]:

$$\varepsilon=\{26.5+14\sigma_{vv}-11\sigma_{hh}-255\log10(\cos\theta)-130\log10(\sin\theta)-21\log10(\lambda)\}\bullet \\ /3.36\tan\theta \tag{4.24}$$

where θ is the incident angle and λ is the wavelength of the incident wave.

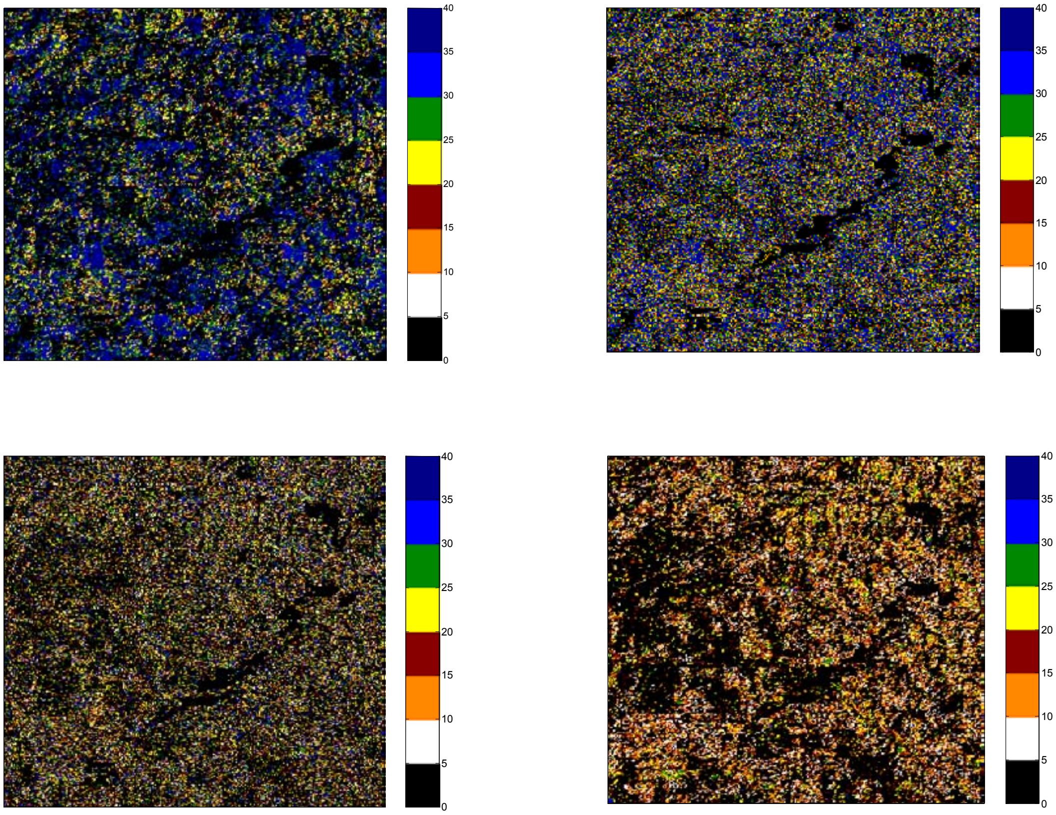

Figure 4.18 Soil moisture maps (Color code unit is percentage) of *Washita'94* site on April 11, 12, 13, & 15, derived using the *Dubois* model showing a general drying trend.

4.2.2.2 *Conclusion*

Since the DM can be applied only to bare soil pixels, *Dubois*. *et al* developed a criteria to eliminate vegetation covered pixels based on the cross-polarized ratio (σ_{hv}/σ_{vv}). They found out that this ratio was a good vegetation index. A regression curve describing the ratio as a function of NDVI is plotted and found out that $\sigma_{hv}/\sigma_{vv} = -11dB$ corresponds to NDVI of 0.4. The algorithm was applied to SIR-C images acquired as part of the *Washita'94* experiment (The pixels with $\sigma_{hv}/\sigma_{vv} > -11dB$ were masked and the inversion algorithm resulted in an *rms* error of 1.6 % for soil moisture when compared to ground truth. From the calculated soil moisture, *rms* height for the area was calculated. In this case, the *rm*se between measured and calculated was 0.15.

The effect of look angle and correlation length, an important surface parameter is not taken in to account. The authors of [1] argue that no correlation is found between these parameters and backscatter coefficients even though IEM model demonstrates strong dependence. It is also pointed out that the correlation length is a difficult parameter to physically measure. The effect of topography is also excluded during the development of the model.

4.3 SHI MODEL (SM)

Both the empirical models discussed in the previous sections (OH & DM) do not take surface power spectrum, or correlation length in to consideration. This is not in agreement with the theoretical model predictions [13]. Another reason, which led to development of the SM inversion algorithm is that the OH & DM are site specific and thus a synthetic data set generated by the IEM model, which covers wider range of surface parameters, is relied upon. This algorithm was applied to SIR-C and AIRSAR measurements acquired over Little Washita watershed in southwest Oklahoma [13]. The *rms* error between measured and calculated *rms* height and soil moisture are found to be 3.4 % and 1.9 dB respectively [13].

4.3.1 Development of Inversion Algorithm

Single scattering IEM model (4.6) can be used to retrieve soil moisture and *rms* height from SIR-C and AIRSAR measurements. Direct application of the IEM model introduces computation inefficiency because of the large size of the SAR data. SAR image is a result of single and multiple reflections. This can result in errors when inverted using the IEM model, because the theoretical model is valid only for single scattering. This is done with the help of target decomposition technique developed for fully parametric data. This mechanism breaks the average covariance matrix in to three decomposed covariance matrices that correspond to single, double and multiple reflections respectively. As a first step the authors simulated the IEM model for a wide range of parameters to study their relationship. Some of their observations are as follows: The relation between σ and m_v is non-linear. σ increases for low values of m_v and gets saturated for high values of m_v. Both σ_{hh} and σ_{vv} do not show much variation with change in m_v for the incident angle range is 30°-50°. The authors of [13] found a good agreement between scatterometer results and IEM model simulations for the trend in backscatter with change in *rms* height. The effect of correlation length increases on backscatter as *rms* height increases.

From the observations and IEM model simulations the authors concluded that IEM model is a potential for inversion of soil moisture from SAR images. The range and step sizes of the IEM parameters used in the generation of the synthetic data are shown in Table 8 [13].

TABLE 8 PARAMETERS USED IN THE GENERATION OF THE SIMULATED DATA

Parameters	*Minimum*	*Maximum*	*Step Size*
Volumetric Soil Moisture	2.0 %	50.0 %	2.0 %
rms height	0.2 cm	3.6 cm	0.2 cm
Correlation Length	2.5 cm	35 cm	2.5 cm
Incidence Angle	25^o	70^o	1^o
Correlation Function	N=1,1.2, 1.4		

A brief note on why the power of correlation functions (N) is chosen to be 1, 1.2 and 1.4 is given in Chapter 3. Most of the natural surfaces fall within the range of 2.5 cm. Thus kh can be considered small (kh=0.78 at L band) and I_{pp}^n of (4.7) can be reduced to the polarization amplitude α_{pp} of the small perturbation model and α_{pp} is given by [13]:

$$\alpha_{hh} = \frac{\varepsilon_r - 1}{(\cos\theta + \sqrt{\varepsilon_r - \sin^2\theta})^2} \tag{4.25}$$

$$\alpha_{vv} = \frac{(\varepsilon_r - 1)(\sin^2\theta - \varepsilon_r(1+\sin^2\theta))}{\left(\cos\theta + \sqrt{\varepsilon_r - \sin^2\theta)}\right)^2} \tag{4.26}$$

The normalized *rms* height is combined with the correlation function to form a new parameter, $S_R = (kh)^2 W$. The inverse normalized backscattering coefficients $|\alpha_{vv}|^2/\sigma_{vv}$, $\left(|\alpha_{vv}|^2 + |\alpha_{hh}|^2\right)/(\sigma_{vv} + \sigma_{hh})$ are simulated using the parameters in Table 8 and their relationship is plotted in Figure 4.19, Figure 4.20, & Figure 4. 21. It is found that small values of S_R have a good linear relationship with the inverse normalized coefficients. An approximate relation between S_R and the inverse normalized coefficients are determined through the regression analysis of the data generated by the IEM model and is given by [13]:

$$10\log 10\left[\frac{|\alpha_{pp}|^2}{\sigma_{pp}}\right] = \alpha_{pp}(\theta) + b_{pp}(\theta) 10\log 10\left[\frac{1}{S_R}\right] \tag{4.27}$$

where $a(\theta), b(\theta)$ are coefficients obtained as a result of regression and for vertical polarization [13]:

$$a_{vv}(\theta) = -6.901 + 5.492\tan(\theta) - 1.051\log(\sin(\theta)) \tag{4.28}$$

$$b_{vv}(\theta) = 0.515 + 0.896\sin(\theta) - 0.475\sin^2(\theta) \tag{4.29}$$

The parameter S_R, which is a function of surface roughness parameters, can be eliminated if both horizontal and vertical polarizations measurements are available.

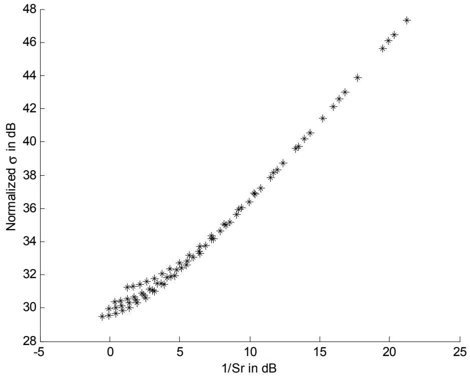

Figure 4.19 Relationship between inverse normalized $|\alpha_{vv}|^2/\sigma_{vv}$ and $1/S_R$ at θ=35°

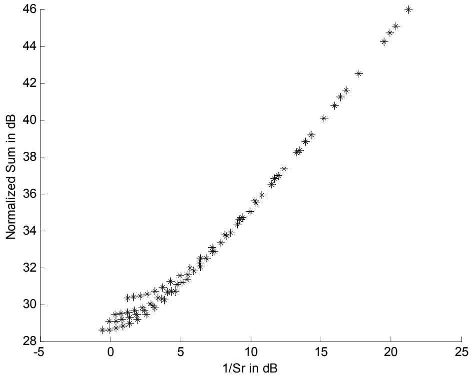

Figure 4.20 Relationship between inverse normalized sum and $1/S_R$

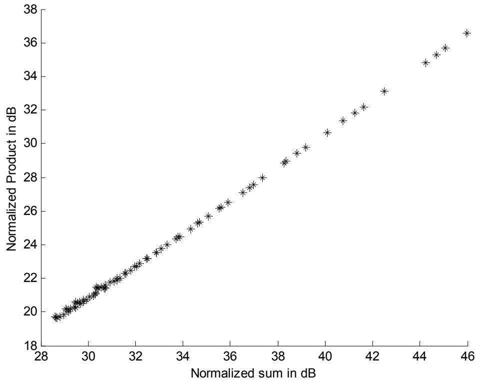

Figure 4. 21 Relationship between inverse normalized sum and inverse normalized product

After replacing S_R with the co-polarized measurements (4.27) can be written as:

$$10\log 10\left[\frac{|\alpha_{pp}|^2}{\sigma_{pp}}\right]=\alpha_{pq}(\theta)+b_{pq}(\theta)10\log 10\left[\frac{|\alpha_{qq}|^2}{\sigma_{qq}}\right] \tag{4.30}$$

The combination of co-polarized coefficients $\sqrt{\sigma_{vv}\sigma_{hh}}$ and $\sigma_{vv}+\sigma_{hh}$ is least sensitive to calibration accuracy and vegetation effects and most sensitive to soil moisture changes [13]. Now, replacing σ_{pp} and σ_{qq} with $\sqrt{\sigma_{vv}\sigma_{hh}}$ and $\sigma_{vv}+\sigma_{hh}$ provides the best for both exponential and Gaussian correlation functions [13]:

$$10\log 10\left[\frac{|\alpha_{vv}|^2+|\alpha_{hh}|^2}{\sigma_{vv}+\sigma_{hh}}\right]=\alpha_{pq}(\theta)+b_{pq}(\theta)10\log 10\left[\frac{|\alpha_{vv}||\alpha_{hh}|}{\sqrt{\sigma_{vv}\sigma_{hh}}}\right] \tag{4.31}$$

The *rmse* between 4.30 and IEM model, and 4.31 and IEM model is found to be 0.35 dB & 0.36 dB respectively [13]. These errors are within the absolute and relative calibration error of SIR-C and hence the SM can be applied to SAR data. These errors increase with larger incident angles [13].

4.3.2 Conclusion

The SAR image is first removed of speckle noise and multiple scattering terms. *Shi. et al.* also employed the DM criteria to remove vegetation pixels. The ε obtained as a result of application of the algorithm is then converted to soil moisture maps using the Dobson model. The *rmse* between the estimated surface soil moisture and *rms* height is found out to be 3.4% and 1.9 dB respectively. The surface roughness parameter is fairly constant during the measurement period [13].

CHAPTER V

METHODOLOGY & DISCUSSIONS

Since the IEM model described in (4.6), is valid only for single scattering terms arising due to surface scattering, it is a requirement to remove multiple scattering terms contributed by vegetation canopies.. At C band, *sparse* vegetation cover can be neglected. The contribution of the soil volume scattering terms is usually neglected because at C band the penetration is less than 2 cm [25]. The vegetation model discussed in this section demands extensive experimental data sets. The model discusses the underlying principle and the variables that influence the vegetation backscatter. Unlike OH and DM, the simplified inversion algorithm developed from the IEM model for surface scattering is not site specific. Finally, the vegetation backscatter determined is deducted from the Radarsat image. This image can then be treated as a backscatter image due to bare soil alone.

5.1 SIMPLIFIED ALGORITHM (USING THE IEM MODEL)

Instead of determining the absolute soil moisture, the algorithm is developed to determine the relative change in soil moisture using Radarsat time series measurements. The estimated relative moisture change can then be coupled with a hydrological model thus improving the accuracy of soil moisture measurement. Since most natural surfaces have a normalized *rms* height of less than 3 cm, multiple scattering terms can be ignored, thus justifying the use of single scattering IEM model. Computational efficiency is the other factor that demands for a simplified form of the IEM model. IEM model cannot be directly used to invert soil moisture because of its complexity and the large volume of SAR data. The algorithms developed in the past [1], [21], [26], have proved that to invert so many unknown parameters, it is necessary to acquire multi-polarized, multi-frequency or multi-incident angle data. Determination of soil moisture is a much simpler problem, given a pixel viewed at different incident angles at the same instant. This section explores the option of multi-incident angle data. Therefore, knowledge about the Radarsat beam mode during collections is critical.

Radarsat has multiple beam modes (S1-S7), which means that it can acquire the region of interest (ROI) at different incident angles, but not at the same instant. Radarsat also has a very brief revisit frequency over the same ROI that is a function of the beam mode. Therefore, this variable revisit frequency of Radarsat can be exploited in the development of the algorithm. The simplified algorithm should be more sensitive to change in dielectric constant and less to surface parameters. It is reasonable to assume that during the Radarsat repeat-passes soil roughness parameters can be considered constant. The temporal variations of surface parameters are small compared to soil moisture during the revisit period [26].

5.1.1 Change Detection Approach

The first approach is the *change-detection* approach [27] with the following assumptions. There should be no change in surface roughness parameters (h,l) during Radarsat revisits. The temporal variation of soil moisture is much larger compared to the above-mentioned parameters, if there is no anthropogenic activity. It is reasonable to assume these parameters are constant between Radarsat repeat-passes. This paper will deal with pixels having range and azimuth dimension of 30m because of the limit in the resolution of Landsat TM.

5.1.1.1 *IEM Model Simulations*

As a first step, the IEM model is simulated with possible combinations of dielectric constant and the ratio of the radar backscatter acquired on the first visit to the backscatter acquired during the second visit. By performing simulations for a wide range of surface roughness, a simplified relation between the radar backscatter and the reflectivity can be developed for *bare soil pixels* using the data set. From the data set generated by the IEM model [28], a simplified algorithm is developed and is given by [29]:

$$\sigma = a(\theta)\Gamma^{b(\theta)} \tag{5.1}$$

where the parameter $a(\theta)$ is dependent on the type of polarization, h, l, and the type of correlation function and $b(\theta)$ depends on incident angle (θ) as it is evident in Figure 5. 1. σ and Γ are radar backscatter and the Fresnel reflection coefficient, respectively. The transmitted and reflected polarization of the incident wave here is horizontal (HH). The correlation function is best determined by plotting the radar backscatter as a function of the incident angle, which is impossible due to the limitations of Radarsat. Plotting σ as a function of θ has to rely either on truck-based scatterometer measurements or assume the correlation function to be exponential or Gaussian. Natural surfaces fall within these functions and here it is assumed to be exponential. One other drawback of the IEM model, apart from being sensitive to the correlation function, is the transition from incident angle to specular angle in the Fresnel reflection term, and this is rectified in [28].

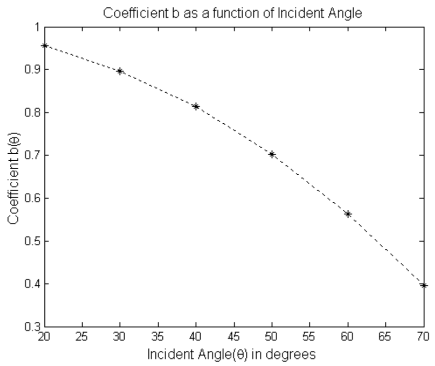

Figure 5. 1 Coefficient b as a function of incident angle

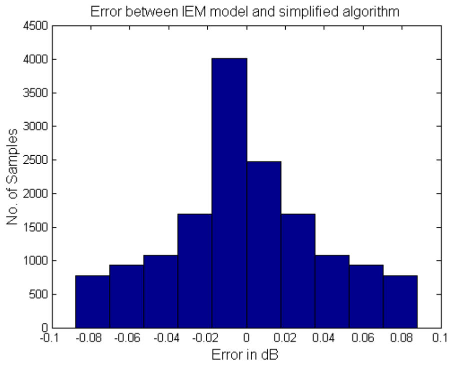

Figure 5. 2 Error between IEM model and (5.2)

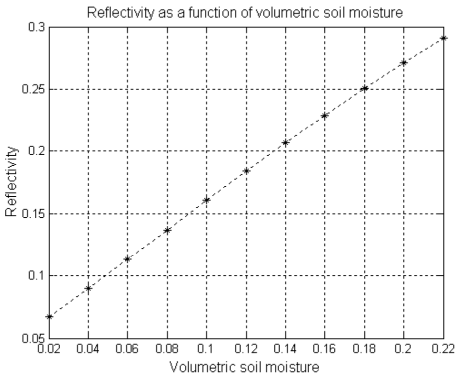

Figure 5. 3 Reflectivity as a function of soil moisture

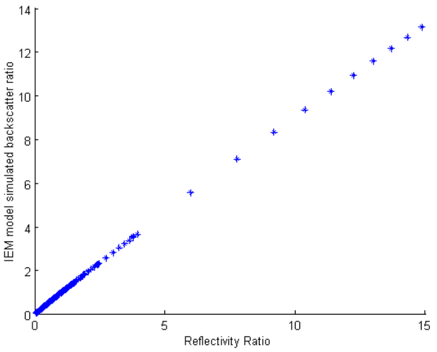

Figure 5. 4 Reflectivity ratio Vs. backscatter ratio

If two visits of Radarsat over the ROI are available at the same incident angle, then their ratios can be written as [29]:

$$\sigma_1 / \sigma_2 = \frac{a(\theta)\Gamma_1{}^{b(\theta)}}{a(\theta)\Gamma_2{}^{b(\theta)}} = \left(\frac{\Gamma_1}{\Gamma_2}\right)^{b(\theta)} \tag{5.2}$$

The term $a(\theta)$ cancels out given the condition that surface roughness remains constant. The parameter $b(\theta)$ can be pre-determined from the IEM model simulations and requires only the knowledge of the incident angle. The reflectivity ratio and backscatter ratio is illustrated in Figure 5. 4. A comparison of the simplified algorithm and the IEM model is shown in Figure 5. 2 and the maximum error ≈ 0.1 dB for $\theta = 20^o$. The error between the relation described in (5.2) and IEM model increases with increase in incident angle. An approximate linear relationship exists between volumetric soil moisture (m_v) and Γ (Figure 5. 3). So, if a change in reflectivity is known then change in soil moisture can be determined.

5.2 VEGETATION MODEL

The vegetation canopy is modeled as a homogeneous layer of scattering particles sandwiched between air and soil. It is important to determine the conditions when the volumetric term is dominant over surface scattering. Research has been conducted that permits the determination of vegetation water content using visible imagery [33]. The key question is how to relate radar backscatter to vegetation water content. Theoretical models have shown that vegetation backscatter is influenced by [30]:

(1) Shape, size and orientation of scattering particles in the canopy

(2) Canopy architecture

(3) Dielectric constant of the scatterers

Since the variables in (1) and (2) vary with crop type, it is difficult to develop theoretical models because of the mathematical complexity. This is the key reason for relying on semi-empirical models. Semi-empirical models determine these variables by varying them in order to minimize the error between the observed and theoretical backscatter in the forward mode. Once these parameters are determined, they can be assumed constant for a crop type and then used for inverting the backscatter. Before proceeding to the underlying principle, some of the assumptions are that the scatterers are spherical, have identical shapes and are uniformly distributed. The terms, as a result of scattering between canopy and ground are neglected. It is known that HH polarized wave gets less affected by vertical scatterers, such as stems than VV polarization. It is not very clear at this point behavior of HH polarization with stalks, though some canopies like wheat have very small amount of total plant water in stalks and their backscatter is neglected [42]. The authors of [42], consider vegetation canopy as a two-layer medium, leaf and stalk scatterers, but for VV polarized wave.

The main principle behind the vegetation model is that the backscatter due to vegetation depends mainly on vegetation water content and crop type (but to a lesser extent). Gravimetric moisture content is defined as the ratio of the mass of the water content in the leaf to the total mass of the leaf [31]. At leaf level, the direct method to retrieve vegetation water mass is to minimize the error between simulated PROPSECT model [32] reflectance and real reflectance for an unknown water content. The difference between simulated reflectance and real reflectance is actually the absorption factor, which is proportional to the water content. This has to be extended to canopy level.

The crop type influence on the backscatter cannot be neglected. According to *Roo. et al.* [29], the total backscatter for a given polarization is given by:

$$\sigma_{total} = \sigma_c + \sigma_{gc-cg} + \sigma_{gcg} + \sigma_g \tag{5.3}$$

where σ_c is the backscatter due to canopy alone, σ_{gc-cg} is the contribution of the *ground-canopy* and *canopy-ground* terms, σ_{gcg} is due to *ground-canopy-ground* interactions and finally σ_g term is the contribution of soil surface alone, but also includes two-way vegetation canopy attenuation. The *ground-canopy-ground* scattering contribution term can be neglected for HH polarization [31]. The following section focuses on the procedure for determination of σ_c alone.

The PROSPECT (Leaf reflectance model) model requires the following inputs for the simulation of the reflectance values for the wavelength ranging from 450 nm to 2500 nm [32]:

- Refractive index (n)
- Leaf Mesophyll structure (N)
- Pigment concentration (C_{ab})
- Effective Water Thickness (EWT).

Equivalent water thickness is defined as the ratio of the total leaf water content per unit area. *Ceccato. et al*. [33], showed that SWIR (Short Wave Infrared) band is a potential for estimation of leaf water content. From the plots below (simulated using PROSPECT model) it is evident that NIR (Near Infrared) region is greatly influenced by changes in leaf structure and chlorophyll content. The reflectance values in the SWIR band are mainly influenced by the leaf structure parameter. Therefore, inverting EWT from SWIR alone will not produce accurate results. Since NIR is also affected by these parameters, it is combined with SWIR to invert EWT. A simple ratio of SWIR to NIR has the potential to derive EWT, at least theoretically. A regression line equation is derived from LOPEX 93 data [33] that related EWT to the simple ratio and is given by:

$$SimpleRatio = 0.666 + \frac{1.0052}{1 + 1159 * EWT} - 6.976 * EWT \tag{5.4}$$

where $SimpleRatio = \dfrac{\rho_{1600}}{\rho_{820}}$ and (5.5)

ρ_{1600}, ρ_{820} are the reflection coefficients at SWIR and NIR respectively.

5.2.1 Atmospheric Correction

At NIR and SWIR bands, aerosol and water vapor are found to affect the reflectance values received by a satellite. This can be resolved by the using the blue band, which is significantly affected by the aerosols.

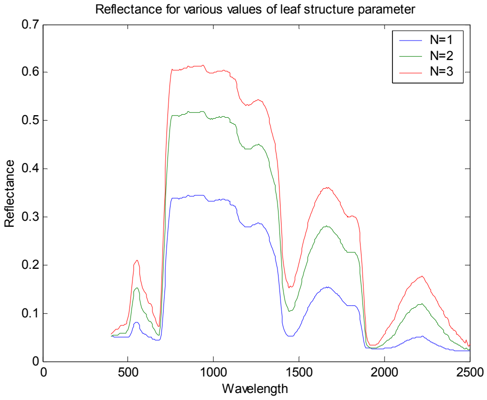

Figure 5. 5 Hyperspectral signature for different leaf structure parameters [32]

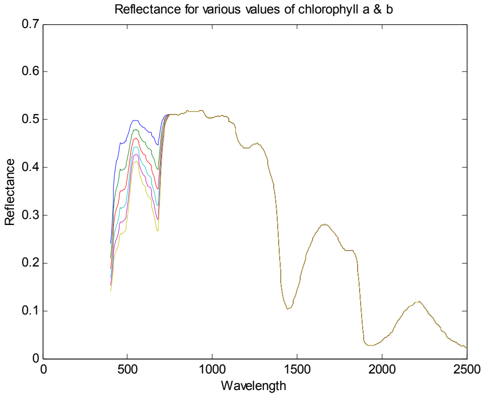

Figure 5. 6 Hyperspectral signature for different pigment concentrations [32]

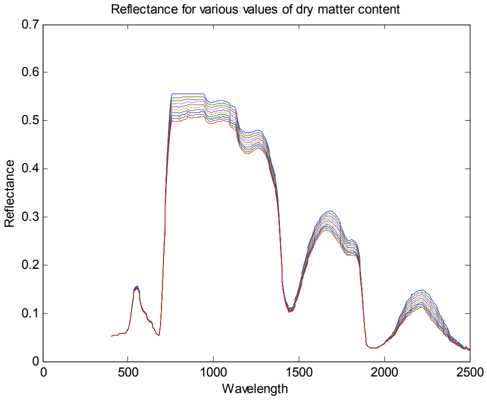

Figure 5. 7 Reflectance for various values of dry matter content (d=0.001 to 0.01)[32]

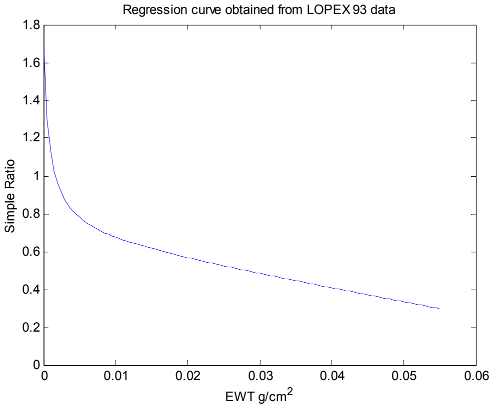

Figure 5. 8 Regression fit derived from LOPEX'93 data set.[32]

The equation used to minimize this effect, is given by *Gobron et al.* [33]:

$$NIRrect = \frac{\left(-1.12(\rho_{blue}+2.169)^2\right)+\left(0.2929(\rho_{nir}+4.2614)^2\right)+\left(65.13\rho_{blues}\rho_{nir}\right)}{\left(-204.3(\rho_{blue}-0.132)^2\right)+\left(0.0109(\rho_{nir}+23.81)^2\right)+\left(5.593\rho_{blue}\rho_{nir}\right)} \tag{5.6}$$

where ρ_{blue} and ρ_{nir} are reflectance normalized by the anisotropic reflectance function and is derived using Rahman, Pinty, Verstraete (RPV) model [34], [33].

5.2.2 Backscattering cross-section of a leaf

This section is mainly a summary of the work done by *Senior et al*. [35]. Their work deals with how gravimetric moisture content of a leaf is related to the backscatter, and extinction cross-sections. Now, the backscatter of a point scatterer is influenced by its shape, orientation, and dielectric properties [35]. Leaves form a major constituent of a canopy and the study of their behavior with incident microwaves has to be understood. A detailed derivation of the relation between the moisture content and backscatter is presented in the paper [35] and only some of their results are presented here.

A leaf can be considered to be a thin layer of dielectric material, with dielectric constant ε, with thickness τ, and it offers a resistivity given by [35]:

$$R = \frac{iZ}{k\tau(\varepsilon - 1)} \tag{5.7}$$

where Z is the intrinsic impedance of free space (377 Ω), k is the propagation constant. The justification for the inclusion of the thickness term is made from the observation that drying of moisture in a leaf is not uniform and its variation with the thickness is given by [35]:

$$\tau = 0.0032m_g^2 + 0.091m_g + 0.075 \tag{5.8}$$

The relation between the gravimetric moisture and dielectric constant is derived from a measured data set obtained at 10 GHz and $22^o c$ [35]:

$$\begin{aligned} \varepsilon' &= 3.95e^{(2.79m_g)} - 2.25 \\ \varepsilon'' &= 2.69e^{(2.15m_g)} - 2.68 \end{aligned} \tag{5.9}$$

The backscatter and extinction cross-section as a result of their derivation is given by [35]:

$$\sigma_{hh} = |\Gamma|^2 \sigma_{pc} \text{ and} \tag{5.10}$$

$$\sigma_{hh}^{ext} = 2A\cos\theta\,\mathrm{Re}(\Gamma) \tag{5.11}$$

where σ_{pc} is the backscatter cross-section of a perfectly conducting plate and Γ is the reflection coefficient for a horizontally polarized wave, A is the area of the leaf. σ_{hh} and σ_{hh}^{ext} are normalized with respect to a perfectly conducting plate and are plotted as a function of m_g in Figure 5. 9 for a leaf of area A=39.5 cm^2. The study in [35], shows that the backscatter and extinction cross-section are mainly a function of moisture content, but are restricted to leaves which are oriented to backscatter specularly from the surface [35], [31].

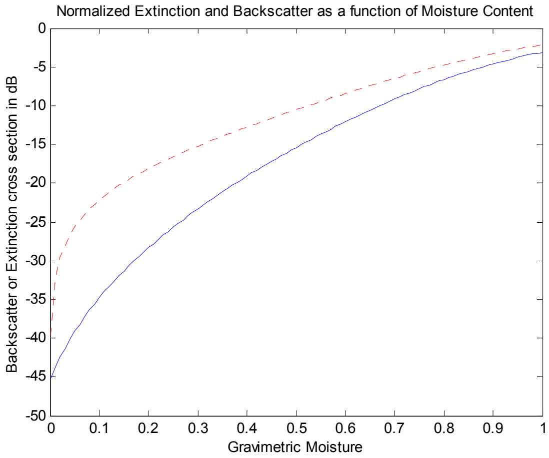

Figure 5. 9 Normalized Extinction and Backscatter as a function of moisture content

5.2.3 Extension of backscatter from a leaf to canopy

The main parameters that affect the reflectance at the canopy level are sensor zenith angle, leaf orientation, Leaf Area Index (LAI), Sun zenith angle and soil. This can be extended to the canopy level simply by:

$$EWTcanopy = EWT \times LAI \tag{5.12}$$

where LAI is the leaf area index, and $EWTcanopy$ is the quantity of water per unit area in the canopy and its unit is gm^{-2}. Based on NIR and SWIR bands, a new index is derived to estimate the vegetation water content [33]:

$$GVMI = \frac{(NIRrect + 0.1) - (SWIR + 0.02)}{(NIRrect + 0.1) + (SWIR + 0.02)} \tag{5.13}$$

The relation between GVMI (Global Vegetation Moisture Index) and $EWTcanopy$ is derived using regression [33]:

$$GVMI = a + \frac{b}{(1 + d(EWTcanopy))} + c(EWTcanopy) \tag{5.14}$$

where a, b, c & d are constants as a result of the regression. The GVMI reaches saturation at $EWTcanopy > 2100\,g\,m^{-2}$. The GVMI is valid for 2 <LAI <5, because of soil effects and the saturation problems associated with LAI. The GVMI and the $EWTcanopy$ for the *Washita'94* experiment site obtained trough Landsat is shown in Figure 5. 10 and Figure 5. 11.

This index is derived for a pixel, where the contribution of both soil and vegetation cannot be ignored from a radar perspective. Thus to validate this statement, a saturation limit in terms of LAI or NDVI has to be determined (In this case LAI is

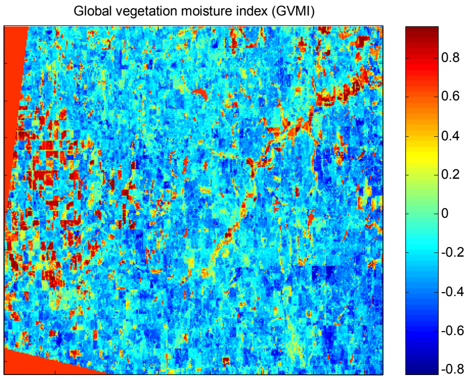

Figure 5. 10 GVMI of *Washita'94* site

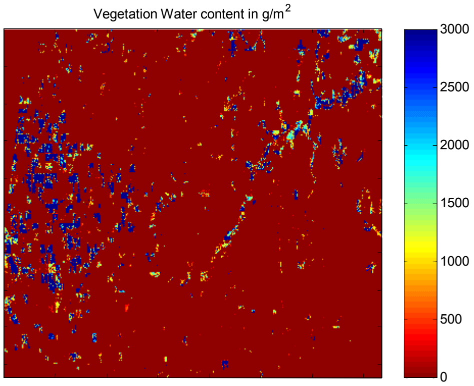

Figure 5. 11 Vegetation water content from GVMI

chosen). When soil backscatter is the dominant term from a single pixel, determination of vegetation moisture content using optical data may be unreliable. This holds true *vice-versa*. Another debate issue is whether to consider the effect of stalks at C band. It was observed that VV polarization underwent considerable attenuation than HH polarization during an experiment conducted in [36].

After finding the moisture content present in vegetation, the next step is to find a relation between m_g and backscatter. Another requirement to do this is to identify the type of vegetation, because backscatter is also influenced by canopy architecture [31].

So the next step involved in the elimination of backscatter due to vegetation is to classify ROI using Landsat imagery based on the crop structure from an SAR perspective [37]. The next section summarizes the classification schemes. This study narrows down the canopy types classified, based on the height or short vegetation and structure. Broad classification of the stems of short vegetation is either *shrub like* or *grass like*. The shrub like vegetation can be further categorized, based on the leaf structure in to *needle-like pods* and *broad leaf* types. Small stemmed can again be classified based on the leaf structure: -*broad* or *blade-like* leaves. Some of the examples of crop types based on the above mentioned classifications are Corn, Wheat and Soybean [37].

5.2.4 A brief overview on classification methods used in *Smex02* site

Supervised classification is used to classify *Smex02* site from Bands 3, 4, 5, & 7 acquired by Landsat [38]. Supervised classification uses samples of known identity to classify unclassified pixels. The most common type of clustering algorithm is the ISODATA algorithm. Initially, the analyst determines n number of clusters using feature vectors in the training data set. Iterations are performed until the cluster means do not vary much from a predefined threshold. The pixels are assigned to each cluster by the Mahalanobis distance measure. There exits parametric and non-parametric classification techniques [39], [40].

5.2.1.1 *Parallelepiped Classifier*

The largest and the smallest digital numbers in bands, usually 3 and 4, or sometimes a set of standard deviations that lie on either side of class means, define rectangular decision areas in two-dimensional scatter plots known as *parallelepipeds*. The pixels are classified by deciding whether they lie in these decision areas and those that do not are labeled *unknown*. This method is computationally efficient but performs badly with classes that exhibit high covariance [39], [40].

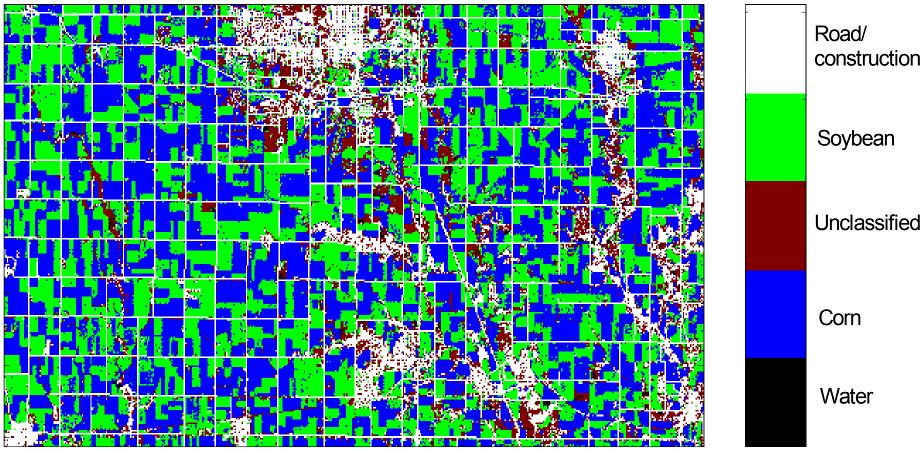

Figure 5. 12 Classified image, Walnut Creek Watershed, Iowa during *Smex02* experiment

5.2.1.2 *Mahalanobis Distance*

Unlike the non-parametric classifier, parametric classifier uses statistical methods parameters such as mean and covariance matrix. A pixel is assigned to a cluster by finding the minimum distance between means of Mahalanobis measure, which is given by (5.15) [40]. The cluster takes an ellipsoidal shape.

$$D = (X_i - m_j)^T C_j^{-1} (X_i - m_j) \tag{5.15}$$

where X_i is the pixel that has to be classified, m_j denotes the mean of the cluster and C_j is the variance-covariance matrix for a cluster. The classified Landsat image is shown in Figure 5. 12.

The main physical parameters that describe the canopy structure are canopy height, shapes and orientation of leaves. According to *Attema*. and *Ulaby*. [41], a vegetation canopy can be modeled as identical water particles bounded by air and soil surface. This *"water cloud"* assumption is based on the findings that the backscatter is mainly a function of dielectric constant due to the vegetation water content in the leaves and stems [42]. Now, neglecting contribution of backscatter from the stems for HH polarization and assuming scattering particles to be uniformly distributed, the backscattering coefficient due to canopy minus the soil contributing term is given by [31]:

$$\sigma^0_{can} = \frac{\sigma_v \cos\theta}{2\kappa_e}\left[1-\gamma^2\right] + \sigma^0_{gc-cg} + \sigma^0_{gcg} \tag{5.16}$$

where, σ_v is the backscattering cross-section per unit volume(m^2/m^3). σ^0_{gc-cg} is the combined contribution of ground-canopy and canopy-ground scattering. This term requires the knowledge of soil reflectivity, which cannot be determined, and thus is neglected from this point forward. σ^0_{gcg} is the ground-canopy-ground scattering contribution and can be neglected for HH polarized waves in the C band [31],

κ_e is the extinction coefficient,

$\gamma = e^{-\kappa_e h \sec(\theta)}$, and

h is the effective canopy height.

5.2.5 Cross-section & m_g Relation

There is a difference in the findings of the relation between moisture content and cross-section coefficients by *Roo. et al.* [31] and *Senior. et al.* [35]. According to *Roo. et al.* [31]:

$$\sigma_v = a_2 m_w / h \text{, and} \tag{5.17}$$

$$\kappa_{hh} = a_4 \sqrt{m_w / h} \tag{5.18}$$

where a_2, a_4 are scattering terms, and are constant for a specific crop type with respect to frequency, polarization. The units of a_2 and a_4 are m^2/kg and $Np/(kg/m)^{1/2}$ respectively.

A non-linear regression program uses an algorithm, such as the Levenberg-Marquardt algorithm that minimizes the LSE between experimental (Where the assumptions when developing 5.3 holds true) and the theoretical backscatter (5.3) to find these free parameters. The values of these parameters for Soybean at C and L band for HH polarization are found in [31], and are shown in Table 9. It is important to establish a database of these parameters for major crop classifications. Both the scattering parameters (a_2, a_4) dominate at C band than at L band. Bistatic scattering contributes to the second term in 5.16, but is less dominating than the backscatter for C band and for L band it is *vice-versa*. The next method is to relate the backscatter cross-section and extinction coefficient to LAI [42].

TABLE 9 FREE PARAMETER VALUES FOR SOYBEAN CROP CANOPY

Frequency	a_2	a_4
C	0.151	0.341
L	0.0	0.126

5.2.6 Cross-section related to LAI

Since the radar backscatter is a strong function of $m_w h$, which in turn are related to the LAI, *Ulaby. et al.* [42], proposed an indirect relation between backscatter and LAI. The authors of the paper [42], also relate the vegetation contribution from a canopy backscatter to the first term of the relation described in (5.16), but do not consider second order or multiple scattering terms. Under the assumption that the canopy can be modeled as a "water cloud", the following relation holds true [42]:

$$\sigma_{can}^{0} = \frac{\sigma_v \cos\theta}{2\kappa_e}\left[1-\gamma^2\right] + \sigma_{stem}^{0} \tag{5.19}$$

where:

$$\frac{\sigma_v}{2\kappa_e} = f(N), \tag{5.20}$$

$$f(N) = A_l[1-\exp(-B_l L/h)] \tag{5.21}$$

where A_l and B_l are constants for a given crop type, incident angle and polarization and L is the LAI. Currently, backscatter from a few vegetation canopies, at VV polarization incident at a specific incident angle is only available. These constants for crop types mentioned previously are tabulated in [42]. It would be interesting to find how the parameters vary for angle and crop types.

5.2.7 Incident Angle Normalization

The variation of local terrain has significant effect on the backscatter, especially in the case of large illumination area, which is the case of a Radarsat image. When dealing with temporal SAR images, it very important to remove the effects of incident angle. Generally we assume the local terrain is relatively flat, hence the local incident angle can be replaced by the incident angle. CCRS (Canada Center for Remote Sensing) initiated a study for compensating the incident angle effects. Three dates of Radarsat images over Manitoba, Canada were acquired [43]. Soil moisture was observed to be constant during these acquisitions. After analysis, the authors of [43] concluded that a change in backscatter per degree ($\Delta\sigma/\theta$) of 0.38 dB is associated with crops and $\Delta\sigma/\theta$ of 0.28 dB for bare pixels for the study area [43]. These results are localized due to limited data set. From prior studies, it was shown that at higher incident angles (>40), shadowing becomes more evident.

The incident angle variation within the resolution cell is minimal and can be ignored. The backscatter as a function of incident angle is dependent of many surface parameters. So, it is important to know the behavior of the backscatter with these parameters. This again forces us to depend on the IEM model (Due to limited availability of SAR images). It is observed that the slope of the backscatter as function of incident angle does not vary much when the dielectric constant changes. This behavioral pattern could be utilized in the elimination of incident angle dependence.

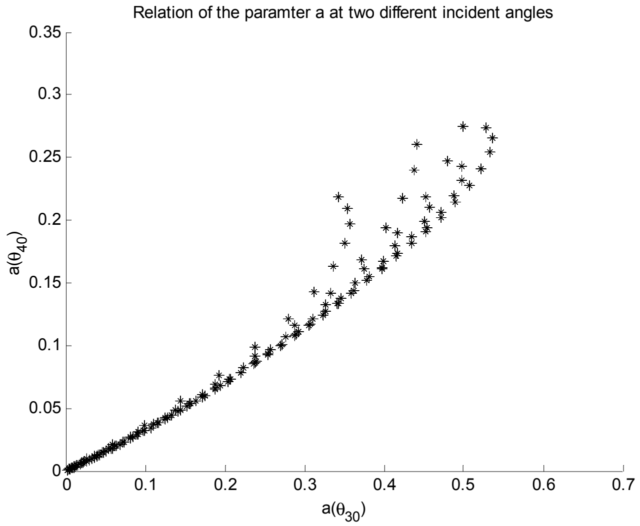

Figure 5. 13 Relation between coefficient $a(\theta)$ at different incident angles 30° and 40°

Normalization of incident angle to a reference angle may be possible at least from an IEM model point of view. For instance, consider two data takes at 30° and 40°. From the IEM model simulations, a regression fits approximately $a(\theta_{30^o})$ to $a(\theta_{40^o})$, which can then be substituted back in the (5.1) to yield $\sigma_{40}{}^{o}$ in terms of $\sigma_{30}{}^{o}$:

$$\sigma_{40^o} = \left(\left(\frac{\sigma_{30^o}}{\Gamma^{b(\theta_{30^o})}} \right)^2 0.3659 + \left(\frac{\sigma_{30^o}}{\Gamma^{b(\theta_{30}{}^o)}} \right) 0.2987 - 0.0004 \right) \Gamma^{\mathrm{b}(\theta_{40^o})} \qquad (5.21)$$

This normalizes $\sigma_{40}{}^o$ to a reference angle 30°, provided surface roughness does not change between data takes. The parameter $b(\theta)$ can be predetermined from IEM simulations. The *rmse* between $\sigma_{30}{}^o$ and $\sigma^o{}_{30/40}$ ($\sigma_{30}{}^o$ obtained from $\sigma_{40}{}^o$) is found to be 0.0048 or 0.74 dB. Since moisture changes between data takes, (5.21) has to be extended to determine relative moisture change. This correction is valid only for surface scattering.

5.3 BACKSCATTER MODEL

The popularity of the backpropagation (BP) algorithm is attributed to its ability of learning functions from multi-dimensional data. BP algorithm uses a gradient search that minimizes the difference between actual and desired outputs [44]. It is a generalization of the minimum mean square error algorithm [44]. Convergence of BP algorithm depends on the initial guess of the weights and bias values [45]. The training cycle is repeated until the cost function is reduced to an acceptable value. The architecture of a Multi-layer perceptron (MLP) network (Figure 5.15) can generally be described as a hierarchal design of interconnected processing units or neurons [46]. A classical architecture consists of an input layer, hidden layer and an output layer and each layer is a collection of processing units. A network may contain more than one hidden layer. The processing units may or may not be fully interconnected. A fully interconnected network is more efficient in learning non-linear functions. The input layer passes on n input vectors without processing to the hidden layer. The hidden layer accepts the input vector and is modeled as shown in Figure 5.14.

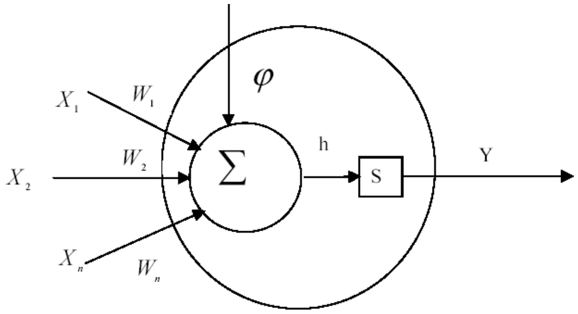

Figure 5.14 Neuron Model

The activation (h) and the output Y is calculated using the following relation [45]:

$$h = w^T x + \varphi \tag{5.22}$$

$$Y = S(y) \tag{5.23}$$

where x is input vector, w represents weight vectors, S is the activation function and is usually sigmoid and φ is an additive bias.

The weights and bias of the BP after each training pattern is updated according to the following rule [45]:

$$\begin{aligned} W_i^{j+1} &= W_i^j + \mu^j \Delta_{W\,i} \\ \Phi_i^{j+1} &= \Phi_i^j + \mu^j \Delta\Phi_i \end{aligned} \tag{5.24}$$

where $\Delta_{W\,i}$ and $\Delta\Phi_i$ are gradient of *rmse* of networks weights and additive bias respectively. μ is the learning rate.

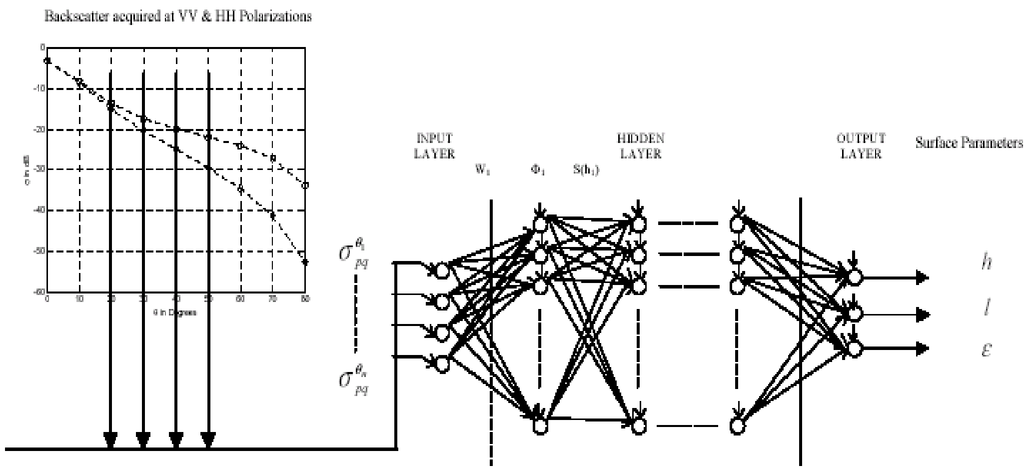

Figure 5.15 MLP Architecture

5.3.1 *Preparing the training data set*

The training data set is formed with a theoretical forward scattering model, IEM model in this case. Since the NN depends heavily on the theoretical model the "correctness" of it has to be ensured. The advantage is that the IEM model is a fairly accurate model and the parameters can be varied freely. The sensitivity of the parameters has to be studied first, in order to leave out of the training patterns to ensure efficient learning [47]. This is done to approximately determine the range of parameters and their step sizes. It is reasonable to consider a maximum of four incident angles because the total revisit time would be a total of 12 days and surface characteristics can be assumed to be constant during this period.

The training data set depends on the practical availability of satellite-induced parameters (frequency, incident angle, polarization). Therefore the forward scattering model has to generate the data set according to this. Theoretically, the following divisions can be made: Based on frequency, polarization, and incident angle, the surface parameters can be inverted by training the network using the IEM model. The main concern is whether it is feasible to obtain SAR data based on the categorization and what would be the drawbacks of each categorization. Researchers in the past have tried to combine these categorizations to improve the efficiency of the inversion algorithm. The popular frequency bands are L, C and X. The first training data set is the data acquired at these bands at one particular incident angle and polarization. Let it be denoted as multi-frequency data. The next possibility is multi-polarized data. Data acquired through HH and VV polarization also can be exploited to determine surface parameters. Data acquired through different incident angles is perhaps the best approach to invert the unknown parameters. The major drawback is that simultaneous multiple viewing is not possible by available SARs.

5.3.2 *SPMA (Single Polarization Multi-Angle) For Radarsat*

A dataset that would match Radarsat acquired data is simulated using the IEM model. The exact incident angles Radarsat acquired during *Smex02* are mentioned in Chapter III.

TABLE 10 PARAMETERS USED IN THE GENERATION OF THE TRAINING DATA SET

Parameters	Training data *min: step size: max*	Test data	*rmse*
h (cm)	0.2:0.4:2.8	0.2:0.5:2.8	0.0073
l (cm)	5:5:25	5:6:25	0.1550
ε	Possible combinations in the range 2:5:25 for 4 incident angles		

The acquired data can be normalized to incident angles $20^o, 30^o, 40^o, 50^o$ using the proposed data. During these acquisitions h, l are constant but dielectric constant may change. Therefore possible combinations of ε are included in the training data set. The network's performance is tabulated in Table 10 for test data set.

The next sections discuss how the surface parameters can be inverted with NN with reasonable accuracy. These categorizations cannot be applied to Radarsat data and are shown for comparison and require simultaneous viewing of the ROI.

5.3.3 *SPMA (Single Polarization Multi-Angle)*

The parameters for training data set for single polarization, multi-angle data (at 20º, 30º, 40º & 50º) are shown in Table 11. A total of 1232 training patterns are fed to the NN. A learning rate and momentum of 0.2 and 0.8 is used during the training and was validated every 50 cycles. A total of 1500 iterations are performed. The number of hidden layers in all the combinations of data set is two, and the number of hidden neurons is 30.

TABLE 11 PARAMETERS USED IN THE GENERATION OF **SPMA** DATA SET

Parameters	Training data *min: step size: max*	Test data	*rmse*
h (cm)	0.2:0.2:2.8	0.3:0.2:2.8	0.0015
l (cm)	2:3:23	3:3:23	0.0286
ε	2:2:22	3:2:22	0.0303

5.3.4 *SAMF (Single Angle Multi-Frequency)*

This combination of input backscatter generated a total of 924 training patterns. A learning rate and momentum of 0.2 and 0.8 is used during the training and are validated every 50 cycles. A total of 1500 iterations are performed. The total number of inputs is 3 (at $\theta = 20^\circ$), which are input backscatter at L, C and X band respectively. The limit in the training data set for h is 1.4 because IEM model is valid for $kh < 3$. The performance is shown in Table 12.

TABLE 12 PARAMETERS USED IN THE GENERATION OF **SAMF** DATA SET

Parameters	Training data *min: step size: max*	Test data	*rmse*
h (cm)	0.2:0.2:1.4	0.3:0.2:1.2	0.0056
l (cm)	2:3:23	3:3:21	0.1441
ε	2:2:22	3:2:20	0.1302

5.3.5 *Single Angle Multiple Polarization (SAMP)*

Combination of both horizontal and vertical polarizations at 20°, generate the data set in Table 13. The number of inputs in this case is 3 and the performance of the NN with respect to h is the poorest.

TABLE 13 PARAMETERS USED IN THE GENERATION OF **SAMP** DATA SET

Parameters	Training data *min: step size: max*	Test data	*rmse*
h (cm)	0.2:0.2:2.8	0.3:0.2:2.7	0.0115
l (cm)	2:3:23	3:3:21	0.1841
ε	2:2:22	3:2:20	0.0930

5.3.6 *Multi-Angle Multi-Polarization (MAMP)*

Keeping in mind the limit Radarsat poses on the number of data takes on the ROI at different incident angles, a maximum of only four different incident angles is considered. Initially, a combination of 2 incident angles at HH and VV polarization, which is a total of 4 inputs, is used as the training pattern. This is increased to 4 incident angles, thus generating a maximum of 8 different backscatter values for the same surface (Table 14). The network architecture for this combination is 8-30-30-3. The *rmse* of the networks discussed are compared in Figure 5.16.

TABLE 14 PARAMETERS USED IN THE GENERATION OF **MAMP** DATA SET

Parameters	Training data	Test data	*rmse* HH, VV, 20^o,30^o	*rmse* HH, VV, 20^o,30^o 40^o	*rmse* HH, VV, 20^o,30^o 40^o,50^o
	min: step size: max				
h (cm)	0.2:0.2:2.8	0.3:0.2:2.8	0.0043	0.0020	0.0017
l (cm)	2:3:23	3:3:24	0.0246	0.0295	0.0251
ε	2:2:22	3:2:20	0.0355	0.0222	0.0158

The performance of the NN (SPMA for Radarsat) trained using a data set generated by IEM model that simulated Radarsat acquisitions is comparable to SAMF and better than SAMP trained NN. By using four incident angles and HH polarization alone, the performance of the NN is comparable to the NN that required both HH and VV observations. It can be concluded that increasing the number of incident angles enhances the inversion of surface parameters. Multi-frequency data limits the data range to which

IEM model can be applied (In terms of h, almost by half at C band) because of the presence of X band.

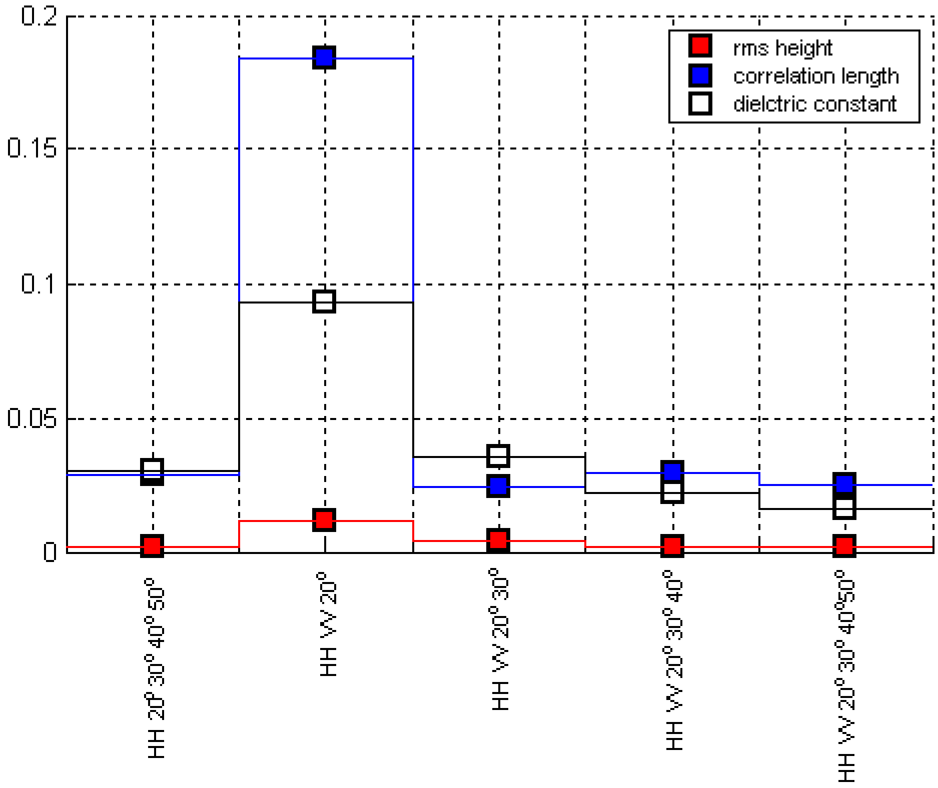

Figure 5.16 *rmse* performance of the BP NN for different input combinations

CHAPTER VI

CONCLUSION & RESULTS

Surface soil moisture can be estimated by measuring the received backscatter from a dielectric such as the soil medium at L, C, & X bands. The dielectric constant of the soil medium in turn is a strong function of soil moisture. From this study, it can be concluded that the science behind the estimation of surface soil moisture and the interactive behavior of the most influencing parameters (*rms* height, correlation length, dielectric constant, surface power spectrum, incident angle) on the radar backscatter are quite well understood. The soil moisture estimation models discussed in this thesis namely, Dubois and Shi models, have reasonable results when applied to SAR data.

Several inversion algorithms, both theoretical and empirical, have been developed to estimate surface soil moisture from radar data. The first theoretical models like the GO & SPM cannot be applied successfully over a wide range of dielectric surfaces. This paved the way for the development of empirical algorithms like the OH & the Dubois model. The OH model is developed from the empirical data sets provided by a truck-based scatterometer, but is unsatisfactory when applied to SAR data. The Dubois model is developed from a similar data set. The model was applied to SAR data during the *Washita'94* experiment and resulted in an *rmse* of 4.2% for the soil moisture estimated. Correlation length, an important surface parameter is not taken into consideration in the Dubois inversion algorithm. To overcome the site-specific problem suffered by the empirical models, the authors of [13] developed an inversion algorithm using a theoretical model called as the IEM model. They improved *rmse* between estimated and observed soil moisture during the *Washita'94* experiment site to 3.4%. All three models estimate soil moisture from multi-polarized data.

This thesis is an effort to develop an inversion procedure (using the IEM model) that completely utilizes the potential of Radarsat and by no means leads to a conclusion that Radarsat is the most effective tool available. The development of a soil moisture inversion algorithm can be approached in two ways: the multiple-incident angle approach and the change detection method. The following observations can be made for consideration for further research and for future soil moisture field campaigns.

In real time, it is difficult to obtain Radarsat data of ROI at the same incident angle with brief revisit time, which calls for an incident angle correction scheme for SAR images. It is possible to normalize the backscatter obtained at different angles to a reference angle from an IEM model standpoint. The *rmse* between backscatter obtained at 30° and the backscatter obtained at 40° normalized to the reference angle 30° using the proposed approach is found to be 0.0048.

IEM simulations show that the surface roughness controls the trend in angular variations of backscatter. SAR images acquired through multiple-incident angles have the potential to map the surface roughness of the ROI, even though dielectric constant varies during the acquisitions. This conclusion is drawn from the performances of the NN when trained using different data sets. Based on prior research, and NN performances, it can be stated that soil parameters can be estimated with reasonable accuracy using a NN if:

- Multi-polarized, multi-frequency or multi-incident SAR data are available

- The network is trained with datasets from a fairly accurate theoretical model like the IEM model.

The current available SARs do not provide multi-polarized or multi-frequency data that is necessary to invert the above-mentioned parameters. However, Radarsat has a very brief re-visit period over the same ROI and this re-visit frequency along with the simplified algorithm discussed in 5.1, [48] is utilized in determining the relative moisture change over the ROI. This method is referred to as *change-detection* method in the literature.

Since the IEM model or the simplified algorithm developed in Chapter V can only be applied on bare soil or scantly covered vegetation pixels, a method has to be developed to eliminate backscatter due to vegetation and interaction with the surface. Combining visible/infrared and microwave region remotely sensed data offers a good potential for elimination of vegetation backscatter. Briefly, the steps involved would be classification of crop type, calculating GVMI from NIR/SWIR bands, relating it to vegetation water content, and determination of backscattering coefficients from the estimated vegetation water content. For pixels covered by vegetation, radar backscatter (apart from surface parameters) is mainly a function of moisture contained in the vegetation, but through a set of free parameters. An extensive database of these free parameters for major crop types (discussed in Chapter V) should be established with the proposed procedure to reduce the effects of backscatter due to vegetation. A method to eliminate the interaction terms between canopy and surface (σ_{gc-cg}) of (5.3)) has to be established. It would be interesting to find out how the free parameters vary with incident angle and crop types. It is proposed that LAI or GVMI can be used indirectly to estimate the backscatter due to vegetation. However, the performance of these two methods has to be compared.

The required data (both satellite & ground) provided by NASA & USDA are still under review and limited distribution, and is expected to be available in September 2003. When the desired ground truth and satellite imagery becomes available, the methodology proposed in this thesis would be applied.

REFERENCES

[1] P. C. Dubois, J. V. Zyl, and T. Engman, "Measuring Soil Moisture with Imaging Radars," *IEEE Trans. Geosciences & Remote Sensing*, Vol. 33, No.4, pp. 915-926 July 1995.

[2] (2003, May) [Online] Available: http://www.ghcc.msfc.nasa.gov/landprocess/lp_home.html

[3] F. T. Ulaby, "Radar measurements of soil moisture content," *IEEE Trans. Antennas Propagation,* Vol. AP-22, pp. 257-265, 1974.

[4] (2003, May) [Online] Available: http://www.sbu.ac.uk/water/explan.html#diel

[5] M. T. Hallikainen, F. T. Ulaby, M C. Dobson, M. A. El-rayes and Lin-Kun Wu, "Microwave dielectric behavior of wet soil- Part 1: Empirical models and experimental observations," *IEEE Trans. Geosciences & Remote Sensing*, Vol. GE-23, No.1, January 1985.

[6] Davidson, M., T. Le Toan, et al, "Measuring the roughness characteristics of natural surfaces soil characteristics of natural surfaces at pixel scales: moving from 1 meter to 25 meter profiles," in *IEEE Int. Geosciences & Remote Sensing Symposium*, (IGARSS'98), Vol. 3, pp. 1200-1201, 1998.

[7] (2003,May) [Online] Available: http://hydrolab.arsusda.gov/washita92/datarpt/chap9.pdf

[8] Charles Elachi, "Radar Remote Sensing: Applications and Techniques," IEEE Press Inc, New York, 1987.

[9] Charles Elachi, "Introduction to the Physics and Techniques of Remote Sensing," John Wiley & Sons, Inc. 1987.

[10] (2003, May) [Online] Available: http://spatialnews.geocomm.com/whitepapers/radarsat1.pdf

[11] J. J. Van Zyl, “Application of Cloude’s target decomposition theorem to polarimetry imaging radar data,” in PIERS Progress in Electromagnetic Research Symposium, 1993.

[12] (2003, May) [Online] Available: http://hydrolab.arsusda.gov/washita94/wash94.htm

[13] Jiancheng Shi, James Wang, Ann Y. Hsu, Peggy E. O’Neill, and Edwin T. Engman, “Estimation of Bare Surface Soil Moisture and Surface Roughness Parameter Using L-band SAR Image Data,” *IEEE Trans. Geosciences and Remote Sensing*, Vol. 35, No. 5, September 1997.

[14] Rajat Bindlesh, “Active & Passive Microwave Remote Sensing of Soil Moisture,” Ph.D. dissertation, The Pennsylvania State University, May 2000.

[15] (2003,May) [Online] Available http://hydrolab.arsusda.gov/Smex02/

[16] F. T. Ulaby, R. K. Moore, A. K. Fung, “Microwave Remote sensing: Active and Passive, 3, From Theory to Applications,” Artech House, 1986.

[17] A.K. Fung, Z. Li, and K. S. Chen, “Backscattering from a randomly rough dielectric surface,” *IEEE Trans. Geosciences. Remote Sensing*, Vol. 30, pp. 356-369, March 1992.

[18] Ji Wu, Liwei Wang, Wei Zhang, Fung A. K, Bo Sun, Suyun Zhu, “Study on soil moisture with ground-based scatterometer and IEM model,” in *IEEE Int. Geosciences & Remote Sensing Symposium*, (IGARSS’01), Vol. 7, pp. 9-13, July 2001.

[19] Fung A. K. “Microwave scattering and emission models and their applications,” Artech House, Inc., 1994.

[20] T. D. Wu, K. S. Chen, J. Shi and A. K. Fung, “A Transition Model for the Reflection Coefficient in Surface Scattering”, *IEEE Trans. Geosciences and Remote Sensing,* Vol. 39, No. 9, pp. 2040-2050, September, 2001.

[21] Y. Oh, K. Sarabandi, F. T. Ulaby, "Empirical model and an inversion technique for Radar scattering form Bare Soil Surfaces," *IEEE Trans. Geosciences and Remote Sensing,* Vol. 30, No.2, pp. 370-381, March, 1992.

[22] Tsan Mo, James R. Wang, Thomas J. Schmugge, "Estimation of surface roughness parameters from Dual-Frequency Measurements of Radar Backscattering Coefficients," *IEEE Trans. Geosciences and Remote Sensing,* Vol. 26, No. 5, pp. 574-579, September 1988.

[23] J. R. Wang, A. Hsu, J. C. Shi, P. E. O'Neill, and E. T. Engman, "A comparison of Soil Moisture Retrieval Models Using SIR-C Measurements over the Little Washita River Watershed," *Remote Sensing of Environment,* Vol. 59, pp 308-320, February 1997.

[24] U. Wegmuller, Lizentiatiasarbeit, Institut fur Angewandte Phsik, Universitat Bern, 1986.

[25] A. Beaudoin, Thuy Le Toan, and H. J. Gwyn, "SAR Observations and Modeling of the C-Band Backscatter Variability Due to Multiscale Geometry and Soil Moisture," *IEEE Trans. Geosciences and Remote Sensing* Vol. 28, No. 5, pp. 886-895, September 1990.

[26] Jiancheng Shi, "Radarsat Report," Unpublished Report.

[27] M. Craig Dobson, Farwaz T. Ulaby, "Active Microwave Soil Moisture Research," *IEEE Trans. Geoscience and Remote Sensing*, Vol. GE-24, No. 1, pp. 23-35, January 1986.

[28] T. D. Wu, K. S. Chen, J. Shi and A. K. Fung, "A Transition Model for the Reflection Coefficient in Surface Scattering", *IEEE Trans. on Geosciences and Remote Sensing,* Vol. 39, No. 9, pp. 2040-2050, September 2001.

[29] Zhen Li, Jiancheng Shi and Huadong Guo, "Measuring soil moisture change with vegetation cover using passive and active microwave data", *IEEE Int. Geosciences and Remote Sensing Symposium*, (IGARSS,'02), Vol. 5, pp. 3071-3073, June 2002.

[30] Rajat Bindlish, Ana P. Barros, “Parameterization of Vegetation Backscatter in Radar-based, soil moisture estimation,” *Remote Sensing of Environment*, Vol. 76, No.1, pp. 130-137, 2001.

[31] Roger D. De Roo, Yang Du, Farwaz T. Ulaby, and M. Craig Dobson, “A Semi-Empirical Backscattering Model at L-Band and C-Band for a Soybean Canopy with Soil Moisture Inversion,” *IEEE Trans. Geosciences and Remote sensing*, Vol. 39, No. 4, pp. 864-872, April 2001.

[32] S. Jacquemoud and F. Baret, “PROSPECT: A Model of Leaf Optical Properties Spectra,” *Remote Sensing of Environment*, Vol.34, pp. 75-91, 1990.

[33] Pietro Ceccato, “Estimation of vegetation water content using remote sensing for the assessment of fire risk occurrence and burning efficiency,” Ph.D. Dissertation, University of Greenwich, November 2001.

[34] Rahman, H., Verstraete, M.M., and Pinty, B., “Coupled Surface-Atmosphere Reflectance (CSAR) Model 1. Model Description and Inversion on Synthetic Data,” *Journal of Geophysical Research*, 98, 20779-20789, 1993.

[35] T. B. A. Senior, K. Sarabandi, and F. T. Ulaby, “Measuring and modeling the backscatter the backscatter cross section of a leaf,” *Radio Science*, Vol. 22, pp. 1109-1116, November 1987.

[36] Tavakoli, A.; Sarabandi, K.; Ulaby, F.T., “Horizontal propagation through periodic vegetation canopies,” *IEEE Trans. Antennas and Propagation*, Vol. 39, No. 7, pp. 1014–1023, July 1991.

[37] Fawwaz T. Ulaby, “Development of SAR Algorithm for Mapping Soil Moisture and Vegetation Biomass,” (February, 1998), [Online] Available: http://lshp.gsfc.nasa.gov/smpreports/ulaby/ulaby.html

[38] Michael Cosh, “SMEX02 Experiment report on Classification of Walnut Creek, Ames, Iowa,” (February 2003) [Online] Available: ftp://hydrolab.arsusda.gov/pub/SMEX02_Data/

[39] Thomas M. Lillesand, Ralph W. Kiefer, “Remote Sensing and Image Interpretation,” John Wiley & Sons Inc., 2000.

[40] Brandt Tso, and Paul M. Mather, “Classification Methods for Remote Sensed Data,” Taylor & Francis, 2001.

[41] Attemma, E. P., Ulaby, F. T. “Vegetation modeled as a water cloud,” *Radio Science*, Vol. 13, pp. 357-364, 1978.

[42] F. T. Ulaby, C. T. Allen, and G. Eger III, “Relating Microwave Backscattering Coefficient to Leaf Area Index,” *Remote Sensing of Environment*, Vol. 14, pp.113-133, 1984.

[43] H. McMairn, R. J. Brown and D. Wood, “Incidence Angle Considerations for Crop Mapping Using Multitemporal Radarsat Data,” Unpublished paper for Canada Center for Remote Sensing.

[44] Xuedong Huang, Alex Acero, Hsiao-Wuen Hon, “Spoken Language Processing,” Prentice Hall PTR, 2001.

[45] Yu Chang Tzeng, K. S. Che, Wen-Liang Kao, and A. K. Fung, “A Dynamic Neural Network for Remote Sensing Applications,” *IEEE Int. Geosciences and Remote Sensing Symposium* (IGARSS’93)*,* Vol. 32, No.5, pp. 514-516, August 1993.

[46] Robert Hecht-Nielsen, “Theory of the Backpropagation Neural Network,” *Proceedings of the International Joint Conference on Neural Networks (IJCNN),* Vol. 1, pp. 593 -605, June 1989.

[47] Michael S. Dawson, Adrian K. Fung, and Michael T. Manry, “A Robust Statistical-Based Estimator for Soil Moisture from Radar Measurements,” *IEEE Trans. on Antennas and Propagation,* Vol. 39, No. 7, pp. 1014 –1023, July 1991.

[48] Zhen Li, Jiancheng Shi and Huadong Guo, “Measuring soil moisture change with vegetation cover using passive and active microwave data”, *IEEE Int. Geosciences and Remote Sensing Symposium*, (IGARSS’02), Vol. 5, pp. 3071-3073, June 2002.